

Globules and pillars in Cygnus X

III. *Herschel* and upGREAT/SOFIA far-infrared spectroscopy of the globule IRAS 20319+3958 in Cygnus X[★]

N. Schneider¹, M. Röllig¹, E.T. Polehampton², F. Comerón³, A.A. Djupvik^{4,5}, Z. Makai^{1,6}, C. Buchbender¹, R. Simon¹, S. Bontemps⁷, R. Güsten⁸, G. White^{2,9}, Y. Okada¹, A. Parikka¹⁰, and N. Rothbart¹¹

¹ I. Physik. Institut, University of Cologne, Zùlpicher Str. 77, 50937 Cologne, Germany
e-mail: nschneid@ph1.uni-koeln.de

² RAL Space, STFC Rutherford Appleton Laboratory, Chilton, Didcot, Oxfordshire, OX11 0QX, UK

³ ESO, Karl Schwarzschild Str. 2, 85748, Garching, Germany

⁴ Nordic Optical Telescope, Rambla José Ana Fernández Pérez 7, 38711 Breña Baja, Spain

⁵ Department of Physics and Astronomy, Aarhus University, Ny Munkegade 120, 8000 Aarhus C, Denmark

⁶ Department of Physics and Astronomy, West Virginia University, Morgantown, WV 26506, USA

⁷ Laboratoire d'Astrophysique de Bordeaux, Université de Bordeaux, CNRS, B18N, allée G. Saint-Hilaire, 33615 Pessac, France

⁸ Max-Planck Institut für Radioastronomie, Auf dem Hügel 69, 53121 Bonn, Germany

⁹ Department of Physics and Astronomy, The Open University, Walton Hall, Milton Keynes, MK7 6AA, UK

¹⁰ SOFIA-USRA, NASA Ames Research Center, MS 232-12, Moffett Field, CA 94035, USA

¹¹ DLR, Rutherfordstraße 2, 12489 Berlin-Adlershof, Germany

August 25, 2021

ABSTRACT

IRAS 20319+3958 in Cygnus X South is a rare example of a free-floating globule (mass $\sim 240 M_{\odot}$, length ~ 1.5 pc) with an internal H II region created by the stellar feedback of embedded intermediate-mass stars, in particular, one Herbig Be star. In Schneider et al. (2012) and Djupvik et al. (2017), we proposed that the emission of the far-infrared (FIR) lines of [C II] at $158 \mu\text{m}$ and [O I] at $145 \mu\text{m}$ in the globule head are mostly due to an internal photodissociation region (PDR). Here, we present a *Herschel*/HIFI [C II] $158 \mu\text{m}$ map of the whole globule and a large set of other FIR lines (mid-to high-J CO lines observed with *Herschel*/PACS and SPIRE, the [O I] $63 \mu\text{m}$ line and the ^{12}CO $16 \rightarrow 15$ line observed with upGREAT on SOFIA), covering the globule head and partly a position in the tail. The [C II] map revealed that the whole globule is probably rotating. Highly collimated, high-velocity [C II] emission is detected close to the Herbig Be star. We performed a PDR analysis using the KOSMA- τ PDR code for one position in the head and one in the tail. The observed FIR lines in the head can be reproduced with a two-component model: an extended, non-clumpy outer PDR shell and a clumpy, dense, and thin inner PDR layer, representing the interface between the H II region cavity and the external PDR. The modelled internal UV field of $\sim 2500 G_0$ is similar to what we obtained from the *Herschel* FIR fluxes, but lower than what we estimated from the census of the embedded stars. External illumination from the ~ 30 pc distant Cyg OB2 cluster, producing an UV field of ~ 150 – $600 G_0$ as an upper limit, is responsible for most of the [C II] emission. For the tail, we modelled the emission with a non-clumpy component, exposed to a UV-field of around $140 G_0$.

Key words. interstellar medium: clouds – individual objects: Cygnus X – molecules – kinematics and dynamics – Radio lines: ISM

1. Introduction

In the vicinity of massive stars, intriguing structures such as column-shaped pillars and cometary-shaped globules are frequently detected in optical as well as near- and far-infrared images (e.g. Schneps et al. 1980; Hester et al. 1996; White et al. 1997; Schneider et al. 2016). They are mostly the result of feedback processes – ionisation and stellar winds – from massive stars and point toward the illuminating source. Larger pillars, however, can also reflect the primordial cloud structure (White et al. 1999; Lefloch et al. 2008; Miao et al. 2009) or arise from eroded convergent flows (Dale et al. 2015). Pillars still have a physical connection to the gas reservoir of the molecular cloud, while globules are isolated features. Figure 1 shows an example

for such objects in the Cygnus X region (Schneider et al. 2016). External UV-radiation creates photodissociation regions (PDRs) on the surfaces of pillars and globules, often visible as a bright rim, facing the ionising source. A rare example of a globule suggested to be also illuminated internally by massive stars is IRAS 20319+3958 in Cygnus X (Schneider et al. 2012, 2016; Djupvik et al. 2017). This source (hereafter, ‘the globule’) is explored in this paper. Other examples of star-formation activity within globules are found in Comerón & Torra (1999). The globule is also impacted by the radiation of the Cyg OB2 cluster located at a projected distance of ~ 30 pc from the globule, assuming that this cluster is located at a distance of 1.4 kpc. It is notoriously difficult to derive distances in Cygnus X, see Schneider et al. (2006); Comerón et al. (2020) for more detailed discussions. We use the value of 1.4 kpc, which is based on maser observations (Rygl et al. 2012) of prominent star-forming sites in Cygnus X.

[★] The [C II] data shown in Figs. 4 and 5 are available in fits format from the CDS via anonymous ftp to cdsarc.u-strasbg.fr (130.79.128.5) or via <http://cdsweb.u-strasbg.fr/cgi-bin/qcat?J/A+A/>.

An analysis of GAIA data (Lim et al. 2020) of Cyg OB2, however, arrived at a larger distance of 1.6 kpc.

Many details of the formation and evolution of globules and pillars have not yet been settled. Numerical modelling started out with simple models of photo-ionisation (e.g. Lefloch et al. 1994) that explained basic properties such as shapes or lifetimes (Johnstone et al. 1998), while the concept of radiative-driven implosion (Bertoldi 1989) provides an explanation of how stars can form in pillars and globules. More realistic models with a careful treatment of heating and cooling processes (e.g. Miao et al. 2006) that consider the turbulent structure of the gas (Gritschneider et al. 2009) and the curvature of the cloud surface (Tremblin et al. 2012a,b) now have the capacity to explain additional properties, such as the velocity field of the observed features. Furthermore, new observations, including *Herschel* imaging and spectroscopy in the far-infrared (FIR) and SOFIA (Stratospheric Observatory for Far-Infrared Astronomy) FIR spectroscopy, make it possible to establish a classification scheme and a possible evolutionary sequence. In the first part of this series of papers (Schneider et al. 2016), we set up a categorisation based on *Herschel* 70 μ m photometry and we propose that pillars advance into globules, which, in turn, evolve into evaporating gaseous globules (EGGs), dense gas condensations without star-formation, or objects with protoplanetary disks (proplyds); or they only resemble proplyds (proplyd-like), depending on density and incident UV-field. In the second paper (Djupvik et al. 2017), we carried out optical and near-IR imaging and spectroscopy of the globule in order to obtain a census of its stellar content and the nature of its embedded sources.

In this work, we present spectroscopic observations of FIR cooling lines of the globule in the southern part of Cygnus X (Reipurth & Schneider 2008), where the very massive and rich Cyg OB2 association illuminates the molecular cloud. The globule was mapped in the [C II] line with SOFIA (Schneider et al. 2012) as well as with *Herschel*/HIFI, PACS, and SPIRE (this paper). It was covered in *Herschel* imaging observations of Cygnus X within the *Herschel* imaging survey of OB Young Stellar objects (HOBYS, Motte et al. 2010) and was also shown and discussed in Schneider et al. (2016). Figure 1 displays a three-colour image of the *Herschel* photometry data with our source indicated.

The objective of this paper is to study the spatial emission distribution of various PDR tracers and to perform a careful analysis of line intensities and ratios using the KOSMA- τ PDR model (Röllig et al. 2006) to disentangle external (Cyg OB2) and internal excitation sources. We intend to show that it is possible to explain most of the observed lines in a PDR model considering the geometry of the source. This approach is more sophisticated than studies that assume plane-parallel, homogeneous layers of gas. There are not many sources holding such a large data set of cooling lines in the mm- to FIR. All the line intensities are given in the accompanying tables and the maps can be provided on demand (the HIFI [C II] data is already provided via CDS, see Sect. 2.1), offering the possibility for other applications and studies.

Another goal is to study the dynamics of the globule. The velocity-resolved extended [C II] map suggests that the globule rotates and that high-velocity outflowing gas escapes from the globule head (some features were shown in Schneider et al. (2012), but not in such detail).

We present the various data sets (*Herschel*, SOFIA, FCRAO, JCMT) in Sect. 2, including a consistency check between FIR line intensities observed with *Herschel* and SOFIA. We give an overview of what is already known about the globule in Sect. 3.

In Section 4, we present the so far unpublished [C II] HIFI and [O I] upGREAT maps of the globule. Section 5 provides details about the PDR modelling and discusses the PDR properties of the globule. Section 6 presents our summary.

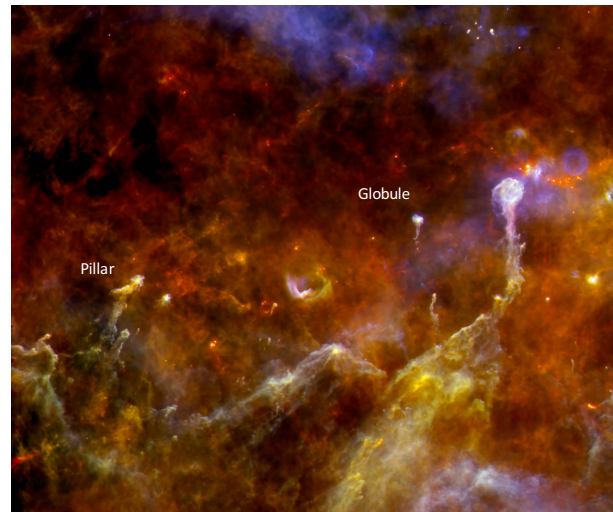


Fig. 1. Three-colour (blue: 70 μ m, green: 160 μ m, red: 250 μ m) image (Schneider et al. 2016) of the environment of Cyg OB2 with the globule IRAS 20319+3958, labeled as 'globule'. The size of the image is $\sim 1.5^\circ \times 1.4^\circ$, which corresponds to ~ 36 pc \times 34 pc, assuming a distance of 1.4 kpc. The pillar indicated further east will be presented in another study. The most massive stars of the Cyg OB2 association are located in the northwest corner of the image (north is up, east to the left).

Table 1. Summary of the HIFI, PACS, and SPIRE spectroscopic observations.

Obsid	Date	α_{J2000} [$^h.m.s$]	δ_{J2000} [$^\circ. ' .''$]	Map size [$''$]
HIFI^a				
1342235079	12/2011	20:33:51.0	40:08:49.0	113.4 \times 110.0
1342244954	04/2012	20:33:48.1	40:06:36.05	97.2 \times 159.5
1342244957	04/2012	20:37:50.0	39:49:23.5	113.4 \times 258.5
1342246343	05/2012	20:37:46.0	39:42:0.0	108.0 \times 132.0
1342246344	05/2012	20:37:42.3	39:51:25.1	135.0 \times 132.0
PACS^b				
1342211184	12/2010	20:33:50.0	40:08:36.0	47 \times 47
1342234987	12/2012	20:37:45.0	39:41:58.0	47 \times 47
1342235855	01/2012	20:37:42.0	39:51:27.0	47 \times 47
SPIRE^c				
1342231073	04/2012	20:33:50.0	40:08:36.2	200 \times 200
1342231074	04/2012	20:33:49.0	40:06:40.2	200 \times 200

Notes. ^(a) The HIFI map covers the whole globule. ^(b) The PACS maps focus on the globule head. ^(c) SPIRE pointed towards a position in the globule head (obsID 1342231073) and the tail (obsID 1342231074).

2. Observations

2.1. *Herschel* spectroscopy

Far-infrared spectroscopic observations of the globule were performed with the *Herschel* Space Observatory (Pilbratt et al.

2010), using the instruments HIFI (de Graauw et al. 2010), PACS (Poglitsch et al. 2010), and SPIRE (Griffin et al. 2010) within the framework of the Herschel Open Time priority 1 project (ot1_nschneid_1) *Pillars of creation: physical origin and connection to star formation* (PI N. Schneider). Table 1 summarises the observational parameters, such as observation date, central position, and map size. All the data is available in the *Herschel* science archive. For convenience, we provide the HIFI [C II] data cube and line integrated intensity at the Centre de données astronomiques de Strasbourg (CDS).

2.1.1. HIFI

The HIFI data consist of Nyquist-sampled, position switched on-the-fly (OTF) maps of the [C II] line at $158\ \mu\text{m}$ with a beam size of $12.2''$ in band 7b at 1910 GHz. We employed the wide-band spectrometer (WBS) with an local oscillator (LO) frequency of 1897.662 GHz. The WBS has a full intermediate frequency (IF) bandwidth of 4 GHz at a spectral resolution of 1.1 MHz (corresponding to a velocity resolution of $0.7\ \text{km s}^{-1}$), in both horizontal (H) and vertical (V) polarisations. The frequency range covered in band 7b is 1892.6 GHz to 1895.2 GHz in the lower sideband (LSB) and 1899.9 GHz to 1902.5 GHz in the upper sideband (USB). The *Herschel Interactive Processing Environment*, (HIPE) version 8.2 was used to remove standing waves and to convert the observed data to CLASS fits-format and the GILDAS packages¹ were used for all further procedures (baseline subtractions, line fittings etc.). In order to obtain a better signal-to-noise ratio (S/N), we averaged the H and V polarisations. The final processed Level 2 data is scaled in T'_A . To scale our data to T_{mb} we multiplied T'_A by the factor of η_l/η_{mb} where η_l is the forward efficiency (0.96) and η_{mb} is the main beam efficiency (0.69) in band 7b. The overall calibration accuracy is $\sim 10\%$ (Roelfsema et al. 2012).

2.1.2. PACS

For the PACS range spectroscopy of the globule head, we used the integral field spectrometer to investigate important cooling lines, namely, the [O I] $63\ \mu\text{m}$ and $145\ \mu\text{m}$ lines, the [N II] $122\ \mu\text{m}$ line, and high-J CO lines. The data were observed in two wavelength ranges: from 51 to $73\ \mu\text{m}$ (blue side) and from 110 to $208\ \mu\text{m}$ (red side). The pipeline processes and all data reduction steps (baseline subtraction, line fitting etc.) were done with HIPE version 7.0 via the built-in pipeline scripts. The line flux measurements were done as described in Schneider et al. (2012), using the PACSman software (Lebouteiller et al. 2012). We note that because the PACS maps are contaminated by emission in the off-position, the calibration was derived only from on-source data and thus associated with a larger error ($\sim 30\%$). For more details, see also Sect. 2.6, where we compare several FIR lines that were observed with *Herschel* and SOFIA. The PACS maps of the globule head are displayed in Fig. A.1 in Appendix A.

2.1.3. SPIRE

The spectra were taken with the SPIRE Fourier Transform Spectrometer (FTS) long and short wavelength receivers (SLW and SSW, respectively) at two positions with sparse sampling. One position is located in the globule head and one in the tail (see Table 1). The SLW observes a hexagonal pattern of 19 spectral pixels (spaxels) covering the wavelength range $313\text{--}671\ \mu\text{m}$ and

the SWS observes 37 spaxels covering $194\text{--}312\ \mu\text{m}$. The beam size at the receiver's central spaxels varies between $16''\text{--}20''$ for SSW and $31''\text{--}43''$ for SLW.

The SPIRE-FTS data were downloaded from the Herschel Science Archive, processed using HIPE v14.1, with SPIRE calibration files `spire_cal_14_3`. The FTS extended source calibration (Swinyard et al. 2014) was used, and in HIPE v14.1, this includes the updates described in (Valtchanov et al. 2018) to align the absolute brightness level to match the SPIRE photometer.

The lines were fitted using the Spectrometer Cube Fitting script in HIPE v15, which carries out a simultaneous fit of the spectral lines and continuum in each band for every spaxel in the spectral cube. The SPIRE maps of the globule head and tail are displayed in Fig. A.2 and A.3 in Appendix A.

2.2. Herschel imaging

We used *Herschel* imaging observation of PACS at $70\ \mu\text{m}$ and $160\ \mu\text{m}$, and SPIRE at $250\ \mu\text{m}$, $350\ \mu\text{m}$, and $500\ \mu\text{m}$ obtained within the HOBYs guaranteed time Key Program (Motte et al. 2010). The angular resolution of the data varies between $6''$ and $36''$ (see Table 2). Column density and dust temperature maps, both at an angular resolution of $36''$, were produced with a pixel-by-pixel SED fit to the wavelengths $160\ \mu\text{m}$ to $500\ \mu\text{m}$ as described in Schneider et al. (2016).

2.3. SOFIA

2.3.1. GREAT: [C II] $158\ \mu\text{m}$ and CO $11\rightarrow 10$

The [C II] $1.9\ \text{THz}$ line and the CO $J=11\rightarrow 10$ molecular rotation line at $1.267\ \text{THz}$ were observed with the PI-heterodyne receiver GREAT² (Heyminck et al. 2012) on SOFIA during one flight on November 10, 2011 from Palmdale, California. OTF maps of the globule, with an angular resolution of $\sim 15''$ for [C II] and $23''$ for CO, were produced. This data set was presented in Schneider et al. (2012). In this paper, we compare the SOFIA [C II] data with what was obtained with HIFI and use the line intensity information of the CO $J=11\rightarrow 10$ line for PDR modelling.

2.3.2. upGREAT: [O I] $63\ \mu\text{m}$ and CO $16\rightarrow 15$

The globule was observed on November 2, 2016, during one flight from Palmdale, California with upGREAT (Risacher et al. 2016) on SOFIA. Only the globule head was covered (map size $\sim 100''\times 80''$), the central position was $\text{RA}(2000)=20^{\text{h}}33^{\text{m}}53.0^{\text{s}}$, $\text{Dec}(2000)=40^{\circ}08'45''$. The seven-pixel HFA array was tuned on the [O I] $4.7\ \text{THz}$ line, the single pixel L2 channel was tuned on the CO $16\rightarrow 15$ line. Both channels observed in parallel, optimised for the [O I] line. We note that the observed CO $16\rightarrow 15$ map thus has missing data points because of the single pixel sampling. The observing mode was chopping single phase A, with a chop amplitude of $100''$ and a chop frequency of $0.655\ \text{Hz}$ with one cycle per dump. The OTF mapping was performed with 1 slew per ref and 6 refs/load. The array orientation was -19.1° . The bandpass averaged system temperature was $2657\ \text{K}$ for the L2 channel and $3512\ \text{K}$ for the H-array. All line intensities are reported as main beam temperatures scaled with main-beam efficiencies of 0.69 and 0.68 for [O I] and CO, respectively, and a

² The German REceiver for Astronomy at Terahertz frequencies. GREAT is a development by the MPI für Radioastronomie and the KOSMA/Universität zu Köln, in cooperation with the MPI für Sonnen-systemforschung and the DLR Institut für Planetenforschung.

¹ <http://www.iram.fr/IRAMFR/GILDAS/>

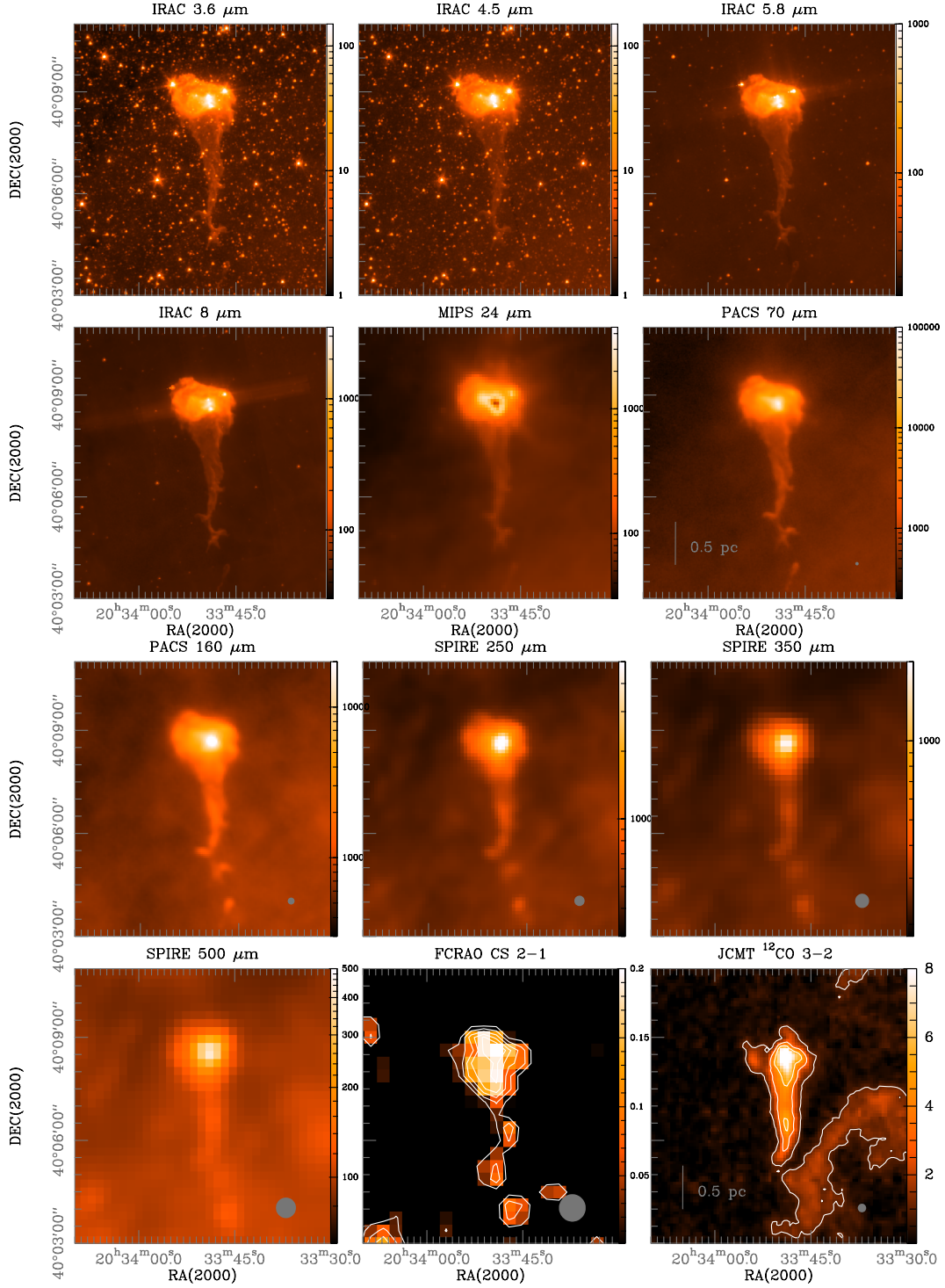


Fig. 2. Globule at IR- and FIR-wavelengths: *Spitzer*/IRAC 3.6 to 8 μm , *Spitzer*/MIPS at 24 μm , *Herschel*/PACS 70, and 160 μm and SPIRE 250, 350, and 500 μm (all units are MJy/sr). The two lower right panels show velocity integrated molecular line emission of CS 2 \rightarrow 1 and ^{12}CO 3 \rightarrow 2 in [K km s $^{-1}$]. The beam is indicated in all panels with longer wavelength observations (starting with PACS 160 μm) in the lower right corner. The *Spitzer* data were already displayed in Djupvik et al. (2017) and the *Herschel* data in Schneider et al. (2016).

forward efficiency of 0.97. The main beam sizes are 15.3'' for the L2 channel (^{12}CO 16 \rightarrow 15) and 6.1'' for the HFA channel ([O I]).

2.4. FCRAO data

We used molecular line data obtained with the 14m dish of the Five College Radio Astronomy observatory (FCRAO), employ-

ing the single sideband focal plane array receiver Second Quabbin Optical Imaging Array (SEQUOIA). The whole Cygnus X region (~ 35 square degrees) was observed in the ^{13}CO 1 \rightarrow 0 at 110.201 GHz, the C ^{18}O 1 \rightarrow 0 at 109.782 GHz, and the CS line at 98.0 GHz. The beamwidth of the FCRAO at 110 GHz is 46''. More details are found in Schneider et al. (2011), where the CO data sets are presented.

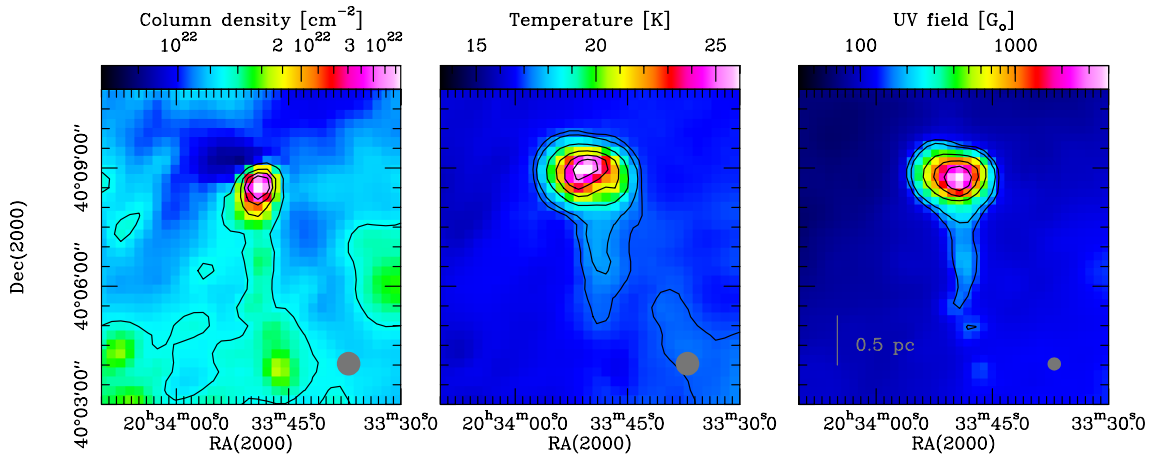


Fig. 3. *Herschel* view of the globule. From left to right: column density (contours 1.3, 1.8, 2.3, 2.8 10^{22} cm^{-2}), temperature (contours 17.1, 17.5, 19, 21, 23, 25 K), and UV-flux map (contours 150, 200, 500, 1000, 2000 G_0) of the globule obtained from *Herschel*. These images are cut-outs from figures shown in Schneider et al. (2016). The column density and temperature maps have an angular resolution of $36''$ and the UV map of $20''$. These resolutions are indicated in the lower right corner of each panel.

2.5. JCMT CO data

The ^{12}CO 3 \rightarrow 2 data used in this paper were obtained with the 16-pixel array HARP receiver in the B-band, and the ACSIS digital autocorrelation spectrometer as the backend correlator system. The individual beams of HARP have a full width at half maximum (FWHM) of $15''$ and the beams are spaced $30''$ apart on a 4×4 grid. The map of the globule is part of the programs M07BU019 (PI R. Simon) and M08AU018 (PI N. Schneider) that were carried out in 2007 and 2008 to map large parts of Cygnus X North and South. The data have a velocity channel spacing of 0.42 km s^{-1} .

2.6. Consistency check between FIR lines observed with PACS, SPIRE, and HIFI (*Herschel*) and (up)GREAT (SOFIA)

The globule is a rare example of a source that was observed in various FIR lines with different instruments on *Herschel* and SOFIA over the last seven years and thus offers the possibility to compare the observed line intensities. The estimated total calibration uncertainties are $\sim 20\%$ for GREAT and upGREAT (Heyminck et al. 2012; Risacher et al. 2016), and 10% for HIFI (Roelfsema et al. 2012). The SPIRE calibration uncertainty for extended sources was estimated to be 7% (Swinyard et al. 2014), although when there is structure in the beam, the uncertainty is larger and dominated by source-beam coupling (Wu et al. 2013). Our data include the latest corrections to match the FTS extended calibration to the SPIRE Photometer (Valtchanov et al. 2018). The PACS data suffer from contamination in the off-position so that the calibration was done only using the on-source data. We thus estimate that the error on the flux is high ($>30\%$) and the observed values are upper limits.

Table 3 shows a comparison between the [C II] 158 μm line, the [O I] 63 μm line, and the CO 11 \rightarrow 10 μm lines, determined at one position in the globule head at RA(2000)= $20^{\text{h}}33^{\text{m}}49^{\text{s}}$, Dec(2000)= $40^{\circ}8'45''$. The flux values obtained for [C II] for HIFI and GREAT as well as the CO 11 \rightarrow 10 line for SPIRE and GREAT agree very well. In contrast, the PACS values for the [C II] and the [O I] line are significantly lower than those obtained with HIFI/GREAT and upGREAT, respectively, which cannot be explained by the PACS contamination problem in the

off-position because the PACS values are upper limits. One explanation can be attributed to positional uncertainties because the [O I] line emission show a large spatial pixel-to-pixel variation and pointing differences can lead to different values. We take the SOFIA [O I] 63 μm data for PDR modelling, but we need to use the PACS [O I] 145 μm data since this line was only observed with *Herschel*. However, this caveat needs to be kept in mind.

3. Multiwavelength observations of the globule

In the following, we shortly present previous works on the globule and summarise the most important physical properties in Table 4.

IR- and FIR-data

Figure 2 displays the globule in the IR- to FIR-wavelength range (3.6 μm to 500 μm , observed with *Spitzer* and *Herschel*), and in the molecular lines of CS 2 \rightarrow 1 and ^{12}CO 3 \rightarrow 2. The IR data show the stellar content of the globule and its environment, while the FIR observations at 70 μm and 160 μm have a too low angular resolution ($6''$ and $11''$, respectively) to resolve the (proto)-stars. The head and tail are well visible at all wavelengths, indicating that there is warm and cold dust present in both. The IR traces the hot PAH dust features while the FIR data longer than 160 μm trace the warm to cold dust. The tail/head ratio flux peaks around 160 μm , but the globule head clearly dominates the emission at all wavelengths. We note that the tail contains no pre- or protostellar sources.

Molecular line data

The two lower right panels of Fig. 2 show that the line-integrated ^{12}CO 3 \rightarrow 2 and CS 2-1 emission arises from the whole globule though the peak of emission is found in the head. The CS emission is more beam diluted because of the lower resolution of $46''$ with respect to CO 3 \rightarrow 2 with $15''$. Interestingly, there is a lack of CO 3 \rightarrow 2 emission in the northeastern globule head, giving the impression that gas was blown out of the centre, leaving this hole. The density of the globule is at least $\sim 10^4$ cm^{-3} if we assume that the molecular line emission is thermalised (Shirley 2015).

Table 2. Summary of the observational data sets of the globule.

Instrument	Species	λ [μm]	ν [GHz]	Δv [km/s]	Θ [$''$]
Herschel spectroscopy					
HIFI	[C II]	157.7	1900.5	0.7	12.2
PACS	[C II]	157.7	1900.5	-	~ 11
PACS	[O I]	145.5	2060.1	-	~ 10
PACS	[O I]	63.2	4744.8	-	~ 9.5
PACS	[N II]	121.9	2459.3	-	~ 9.4
PACS	$^{12}\text{CO } 16 \rightarrow 15$	162.8	1841.4	-	~ 11.5
PACS	$^{12}\text{CO } 14 \rightarrow 13$	186.0	1611.8	-	~ 12.5
PACS	$^{12}\text{CO } 13 \rightarrow 12$	200.3	1496.9	-	~ 13
SPIRE	[C I]	370.4	809.3	-	34.8
SPIRE	[C I]	609.1	492.2	-	37.2
SPIRE	[N II]	205.2	1461.1	-	16.9
SPIRE	$^{12}\text{CO } 13 \rightarrow 12$	200.3	1496.9	-	16.8
SPIRE	$^{12}\text{CO } 12 \rightarrow 11$	216.9	1382.0	-	17.2
SPIRE	$^{12}\text{CO } 11 \rightarrow 10$	236.6	1267.0	-	17.6
SPIRE	$^{12}\text{CO } 10 \rightarrow 9$	260.2	1152.0	-	17.7
SPIRE	$^{12}\text{CO } 9 \rightarrow 8$	289.1	1036.9	-	19.2
SPIRE	$^{12}\text{CO } 8 \rightarrow 7$	325.2	921.8	-	36.8
SPIRE	$^{12}\text{CO } 7 \rightarrow 6$	371.7	806.7	-	34.8
SPIRE	$^{12}\text{CO } 6 \rightarrow 5$	433.6	691.5	-	29.4
SPIRE	$^{12}\text{CO } 5 \rightarrow 4$	520.3	576.3	-	32.6
SPIRE	$^{12}\text{CO } 4 \rightarrow 3$	650.3	461.0	-	40.4
SPIRE	$^{13}\text{CO } 9 \rightarrow 8$	302.4	988.8	-	36.1
SPIRE	$^{13}\text{CO } 8 \rightarrow 7$	340.2	881.3	-	36.1
SPIRE	$^{13}\text{CO } 7 \rightarrow 6$	388.7	771.2	-	34.0
SPIRE	$^{13}\text{CO } 6 \rightarrow 5$	453.5	661.1	-	30.0
SPIRE	$^{13}\text{CO } 5 \rightarrow 4$	544.2	550.9	-	32.9
Herschel photometry					
PACS	continuum	70	4283	-	6.0
PACS	continuum	160	1874	-	11.4
SPIRE	continuum	250	1199	-	17.8
SPIRE	continuum	350	857	-	25.0
SPIRE	continuum	500	600	-	35.7
SOFIA					
GREAT	[C II]	157.74	1900.5	0.23	15.1
GREAT	$^{12}\text{CO } 11 \rightarrow 10$	236.61	1267.0	0.69	22.5
upGREAT	[O I]	63.18	4744.8	0.25	6.1
upGREAT	$^{12}\text{CO } 16 \rightarrow 15$	162.81	1841.4	0.64	15.3
FCRAO					
SEQUOIA	$^{13}\text{CO } 1 \rightarrow 0$	2720.4	110.2	0.067	45
SEQUOIA	CS $2 \rightarrow 1$	3059.1	98.0	0.075	48
JCMT					
HARP	$^{12}\text{CO } 3 \rightarrow 2$	869.0	345.8	0.42	15

Notes. The first column gives the instrument, the second the line (or continuum), the third and forth the wavelength and frequency, the fifth the velocity resolution used in this paper, and the six column the angular resolution. We note that the PACS and SPIRE FIR lines are not spectrally resolved and that the SOFIA and FCRAO line observations were smoothed to a lower velocity resolution when used in displays of spectral line maps or channel maps. For PDR-modelling, we smoothed all data sets with an angular resolution higher than $20''$ to a common value of $20''$.

Herschel column density and temperature maps and the UV field

High (column) densities are confirmed by the *Herschel* dust column density map (Fig. 3, left panel), which indicates peak values of a few 10^{22} cm^{-2} for the globule head, (see also Schneider

Table 3. Comparison of line integrated intensities.

	[C II] 158 μm [K km s $^{-1}$]	[O I] 63 μm [K km s $^{-1}$]	$^{12}\text{CO } 11 \rightarrow 10$ [K km s $^{-1}$]
SPIRE/ <i>Herschel</i>	-	-	27.0 @ 17.6''
PACS/ <i>Herschel</i>	68.0 @ 16''	4.0 @ 16''	-
HIFI/ <i>Herschel</i>	108.5 @ 12''	-	-
GREAT/SOFIA	107.3 @ 15''	-	27.2 @ 22''
upGREAT/SOFIA	-	10.6 @ 16''	-

Notes. The line integrated intensities are given in main beam brightness temperatures with different angular resolutions at one common position at RA(2000)= $20^{\text{h}}33^{\text{m}}49^{\text{s}}$, Dec(2000)= $40^{\circ}8'45''$ in the globule head for each line in the globule observed with SPIRE, PACS, HIFI (*Herschel*), and GREAT or upGREAT on SOFIA.

Table 4. Physical properties of the globule in total (column 2) and the head and tail (column 3 and 4), respectively.

	Globule	Globule head	Globule tail
$\langle N \rangle$ [10^{21} cm^{-2}]	14.2	14.3	14.0
Mass [M_{\odot}]	238	166	73
Density [10^3 cm^{-3}]	6.5	5.2	7.7
$\langle T \rangle_{\text{dust}}$ [K]	19.7	19.7	17.0
Length [pc]	1.78	0.85	0.93
Width [pc]	0.3-0.9	0.9	0.3
Area [pc^2]	0.9	0.62	0.28
average UV-field [G_{\odot}]		550	170
peak UV-field [G_{\odot}]		4300	220
incident UV-field [G_{\odot}]	150-600	150-600	150-600

Notes. The values were derived from the *Herschel* column density and temperature maps (Schneider et al. 2016). A distance of 1.4 kpc was assumed, so that $1'$ corresponds to 0.4 pc. The area is the equivalent area of a polygon used to derive the mass, density etc. $\langle N \rangle$ is the average H_2 column density. The average and peak flux values were derived from the *Herschel* fluxes, explained in Schneider et al. (2016), the incident UV-flux from a census of the stars from Cyg OB2.

et al. 2016), where the column density map, temperature map, and UV-field map were already shown for a larger area and the globule was labelled 'g1' in region 1-3. The values for average H_2 column density $\langle N \rangle$, mass M , average density n , length and width, and dust temperature T are given in Table 4. We note that we averaged across the whole head as it was originally defined (Schneider et al. 2016) by $70 \mu\text{m}$ emission, which corresponds to the area seen in the temperature map. The average values for column density and density are thus lower than as if we would have only taken the high column density area seen in Fig. 3. The temperature, also determined from an SED fit to the *Herschel* data, is 19.7 K, but shows a strong variation from 17.2 K south of the globule centre to 26.3 K at the centre of the globule head (Fig. 3, middle panel).

From the *Herschel* $70 \mu\text{m}$ and $160 \mu\text{m}$ flux, Schneider et al. (2016) calculated an average UV flux across the globule head of $\sim 550 G_{\odot}$ (in units of the Habing field³) and a peak value (in a $20''$ beam) of $\sim 4300 G_{\odot}$. From a census of the exciting stars of the Cyg OB2 cluster, the incident UV-field on the globule is only 150-600 G_{\odot} (not accounting for extinction by the molecular

³ Note that the Habing field G_{\odot} relates to the Draine field χ by $\chi = 1.71 G_{\odot}$ where G_{\odot} is the mean interstellar radiation field from Habing (1968); Draine (1978). We use both measures in this paper.

clouds of the Cygnus X region and ignoring projection effects). We thus anticipate that internal sources must also contribute to the measured UV field from the *Herschel* fluxes.

Stellar content inside the globule

Earlier studies reported nine cluster members within a projected radius of ~ 0.5 pc (Kronberger et al. 2006; Kumar et al. 2006) and two visible stars had been estimated to have mid-B spectral types (Cohen et al. 1989). The scenario of embedded stars was further explored in Djupvik et al. (2017), where we found that the globule contains an embedded aggregate of about 30-40 young stellar objects within one arcmin (or 0.4 pc with the adopted distance of 1.4 kpc). Based on the high ratio of Class I to Class II objects, the small cluster was estimated to have an age < 1 Myr. The most massive members were designated stars A, B, and C. Star A was discovered to be a binary with one component being a Herbig Be star with an estimated mass of $13 M_{\odot}$. Star B was found to have spectral type B0.5 to B1.5 and an estimated mass of $23 M_{\odot}$. The bright mid-IR Class I source, Star C, was resolved in a binary, of which at least one is a massive YSO of spectral type late O or early B with $8.1 M_{\odot}$. Optical spectroscopy of the nebula next to these stars revealed clear signs of a low-excitation H II region, as one would expect from early B-type stars rather than the harder radiation from O stars in the nearby Cygnus OB2 association. Furthermore, the morphology seen in high-angular-resolution images of H₂ line emission tracing the PDR, and Br- γ line emission tracing the ionised gas, was interpreted as additional evidence that the globule is illuminated from the inside.

4. Results and analysis

Here, we present a study of many cooling lines in the mm- to FIR-wavelength range, which all arise from photodissociation regions (PDRs). The hot ($T > 100$ K) PDR component is best traced in the cooling lines of atomic oxygen ([O I] at 63 and 145 μ m) and high-J CO rotational lines. The warm ($T \sim 100$ K) layer of the PDR is seen in the 158 μ m line of ionised carbon, followed by the fine-structure lines of neutral carbon ([C I] 1 \rightarrow 0 and 2 \rightarrow 1 at 609 μ m and 370 μ m, respectively). The cool ($T < 50$ K) molecular cloud is traced in low-J CO lines. Apart from the gas temperature and UV field, it is also the density in the PDR that determines which of the lines is the dominant cooling line. It is a major challenge to correctly reproduce the observed line intensities in PDR models. Some models focus on establishing a careful chemical network, while others emphasise geometrical effects, such as considering the inhomogeneous structure of the PDR (e.g., Tielens & Hollenbach 1985; Black & van Dishoeck 1987; Le Boulton et al. 1993; Kaufman et al. 1999; Sternberg & Dalgarno 1995; Wolfire et al. 2003; Meijerink & Spaans 2005; Röllig et al. 2006; Bisbas et al. 2015). Röllig et al. (2007) and Bisbas et al. (2015) give an overview of the various PDR codes with a comprehensive reference list.

4.1. *Herschel*/HIFI [C II] 158 μ m emission distribution

Figures 4 and 5 show the spatial and velocity distribution of the [C II] emission in the globule observed with HIFI on *Herschel*. The overall emission in the globule head is similar to what was found in Schneider et al. (2012), based on GREAT/SOFIA observations. We note that the globule tail was not observed with SOFIA in 2012. The channel maps (Fig. 5) reveal the correlation between [C II] emission and the stellar content. Star A (the

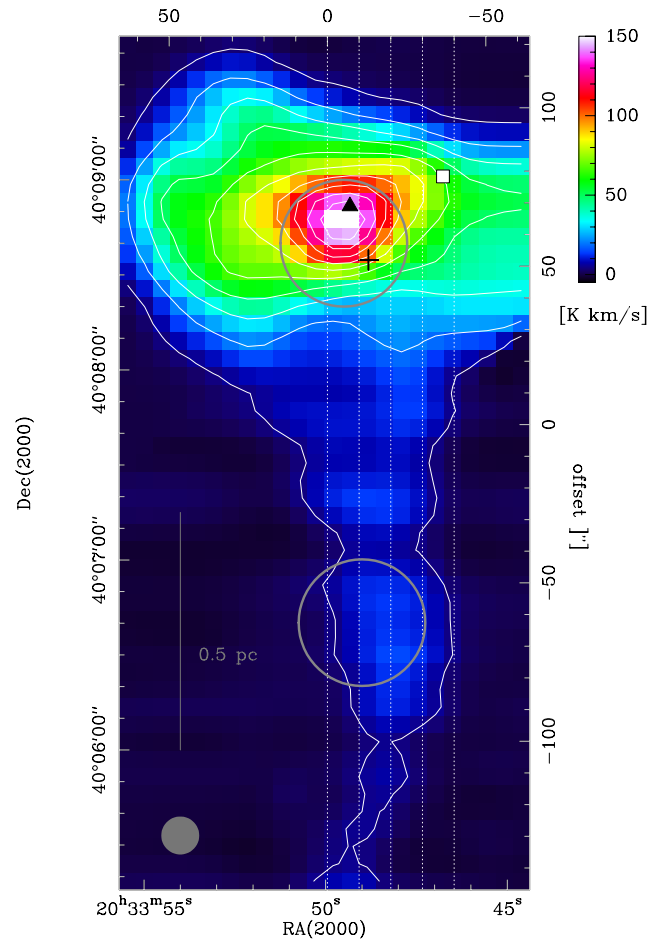


Fig. 4. Line-integrated [C II] 158 μ m emission of the globule obtained with HIFI on *Herschel* in the velocity range 0 to 15 km s⁻¹. The black triangle indicates the double system (Star A) of which at least one is a Herbig Be star, the white rectangle points to Star B with a B0.5 - B1.5 spectral type, and the black cross marks Star C, a resolved binary of which one is a late O or early B star. The centre position (0,0) is at RA(2000)=20^h33^m49.95, Dec(2000)=40°07'42.75". The [C II] beam is indicated in the lower left corner. The dashed lines indicate the vertical (north-south) cuts where we performed position-velocity maps and the dark grey circles mark the positions and the extend of the SPiRE beam for the longest wavelengths (FWHM $\sim 40''$) we used for PDR modelling. The position in the north is the globule 'head' and the one in the south the globule 'tail'.

Herbig Be star, black triangle) displays a clear correlation between high velocity [C II] emission in the blue (2.5-5.3 km s⁻¹) and red (11.6-13 km s⁻¹) velocity range. We observe outflowing gas from the inner PDR region around Star A that had already created a small cavity because of its stellar wind and radiation (Schneider et al. 2012). This point is discussed in more detail in Sect. 4.4. Interestingly, the two other star systems do not display a strong correlation with [C II] emission. Star B (the single early B-star, white rectangle) lies outside of significant [C II] emission for all velocity channels, while Star C (binary with a late O star, grey cross) can also serve as an exciting source for ionising carbon in the PDR region. The channel maps show that the bulk emission of the globule between ~ 6.7 km s⁻¹ and 10.2 km s⁻¹ has first a prominent peak enclosing the three stellar systems, then forms an arc-like structure ($v=8.1$ km s⁻¹) and then develops a single peak south-east of the stars.

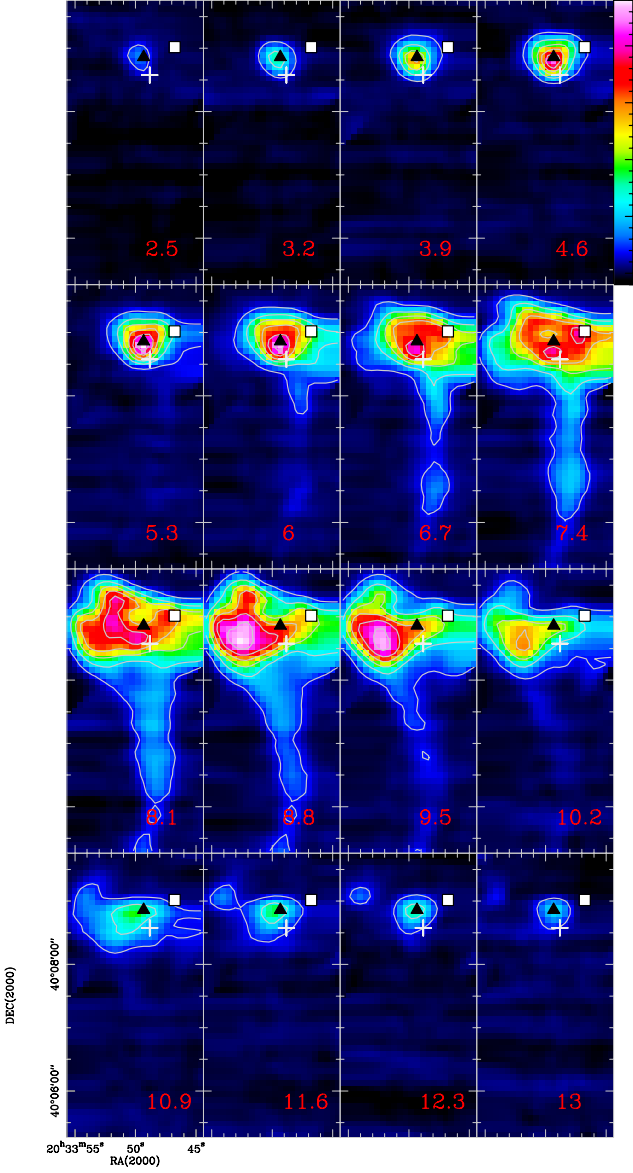


Fig. 5. Channel maps of [C II] emission obtained with HIFI on *Herschel* from 2.5 km s^{-1} to 13 km s^{-1} . The symbols indicate the three stellar systems, similar to Fig. 4, except that here Star C is indicated with a white cross for better visibility.

The globule tail is fainter in [C II] emission. The integrated intensity in the tail (Fig. 4) is typically $\sim 10 \text{ K km s}^{-1}$, which is a factor of 10-15 smaller than what is found in the globule head. Nevertheless, this level of [C II] emission indicates that there is some external heating (there are no exciting sources in the tail) from the overall FUV field around the globule, mostly caused by the Cyg OB2 cluster.

4.2. [C II] column density and mass

We calculate the mass associated to the gas traced by [C II] emission using a simplified version of the formula for the [C II] column density in the limit of optically thin emission given by Eq. 2 in Langer et al. (2010) or Eq. 26 in Goldsmith et al. (2012) that

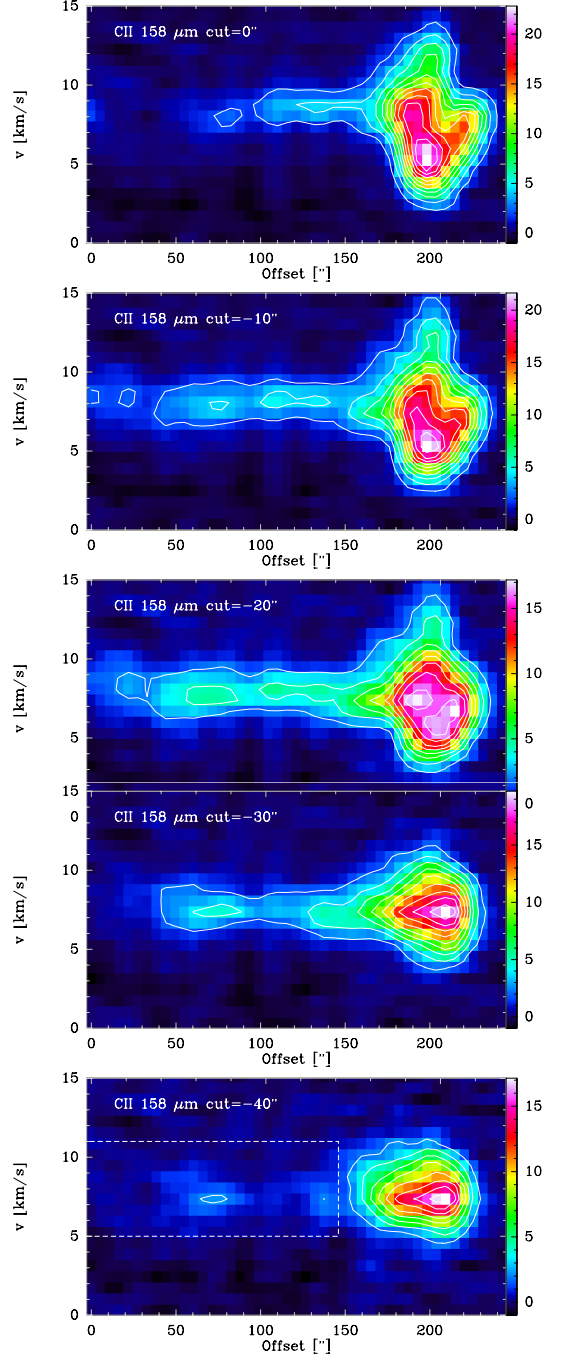


Fig. 6. Position-velocity maps of the globule in [C II] for 5 vertical cuts in declination at different RA offsets, indicated in Fig. 4. The zero-offset is at $\text{RA}(2000) = 20^{\text{h}}33^{\text{m}}50^{\text{s}}$ and goes then in steps of $10''$. The Dec (2000) range is $40^{\circ}05'15''$ to $40^{\circ}09'45''$. The bottom panel for cut= $-40''$ outlines with a white dashed rectangle the globule's tail for which we show an overlay between two PV cuts in Fig. 7.

is

$$N(\text{C}^+) = 2.9 \times 10^{15} \left(1 + 0.5 e^{91.25/T_{\text{kin}}} \left(1 + \frac{2.4 \times 10^{-6}}{R_{\text{ul}} n} \right) \right) I(\text{C}^+) [\text{cm}^{-2}], \quad (1)$$

with R_{ul} as the collisional de-excitation rate coefficient at a kinetic temperature T_{kin} and density n of the collisional partner, which may be either electrons or atomic or molecular hydrogen.

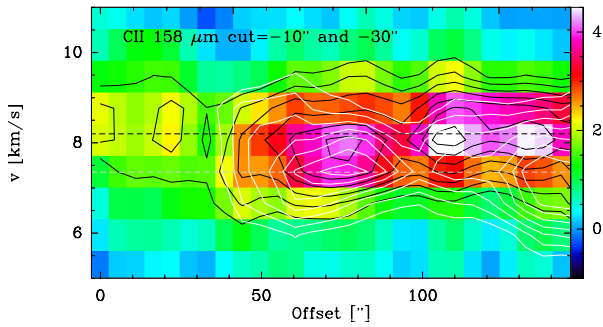


Fig. 7. Overlay between PV maps of the globule in [C II] for the $-10''$ (black contours) and $-30''$ (white contours) vertical cuts, indicated in Fig. 4. The dashed lines show the centre velocity of the globule's tail for the cuts, i.e. 8.20 km s^{-1} for the $-10''$ cut and 7.35 km s^{-1} for the $-30''$ cut, respectively.

In addition, $I(\text{C}^+)$ is the line integrated observed [C II] intensity. As a first-order approximation, we assume high kinetic temperatures and high densities, so that this equation is simplified to:

$$N(\text{C}^+) = 4.38 \times 10^{15} I(\text{C}^+) [\text{cm}^{-2}]. \quad (2)$$

We distinguish between the gas entrained in the outflow in the globule head, namely, [C II] emission in the blue ($v=0$ to 5 km s^{-1}) and red ($v=12$ to 15 km s^{-1}) velocity range, and the bulk emission ($v=5$ to 12 km s^{-1}). For the bulk emission, we derive an average [C II] column density of $2.0 \times 10^{17} \text{ cm}^{-2}$ and $0.4 \times 10^{17} \text{ cm}^{-2}$ for the globule's head and tail, respectively. Assuming an abundance of $\text{C}/\text{H} = 1.2 \times 10^{-4}$ (Wakelam & Herbst 2008), we estimate a mass of $\sim 13.63 M_{\odot}$ and $\sim 1.55 M_{\odot}$ for the globule head and tail, respectively. The gas mass in the outflow is $1.57 M_{\odot}$ and $0.68 M_{\odot}$ for the blue and red velocity range, respectively. We note that the masses derived from [C II] are lower limits and lower than what was derived from the dust. However, the values are not directly comparable. While dust emission is optically thin and traces all gas along the line-of-sight, the [C II] emission can be optically thick and arise mostly from the PDR surface.

4.3. Large-scale dynamics of the globule

The dynamics of the globule head was already discussed in Schneider et al. (2012). We confirm with the HIFI [C II] data the detection of a velocity gradient and differences in line position and width within the globule head (cf. Fig. 5). Figure 6 displays position-velocity (PV) plots for five vertical cuts through the whole globule that are indicated in Fig. 4. The cuts at offsets 0 and $-10''$ cross Star A and we observe - similar to the channel maps - high velocity blue- and red-shifted emission and an opening in the globule head with an arc-like structure. The cuts further away from Star A show more confined emission spatially and kinematically and reflect the primordial velocity structure of the globule with gas around 7 km s^{-1} . The globule tail does not show a velocity gradient along its main axis (north-south orientation) in the individual cuts, but there is an east-west velocity gradient. This becomes obvious in an overlay between the emission in the cuts at $-10''$ and $-30''$ (Fig. 7) and is also seen in the channel maps of Fig. 5. The 'blue' part of the [C II] tail at 7.4 km s^{-1} is located further west compared to the 'red' part of the [C II] tail visible at higher velocities around 8.1 – 8.8 km s^{-1} .

Figure 8 displays the velocity pattern of the whole globule in more detail, this time including the tail, which was not observed

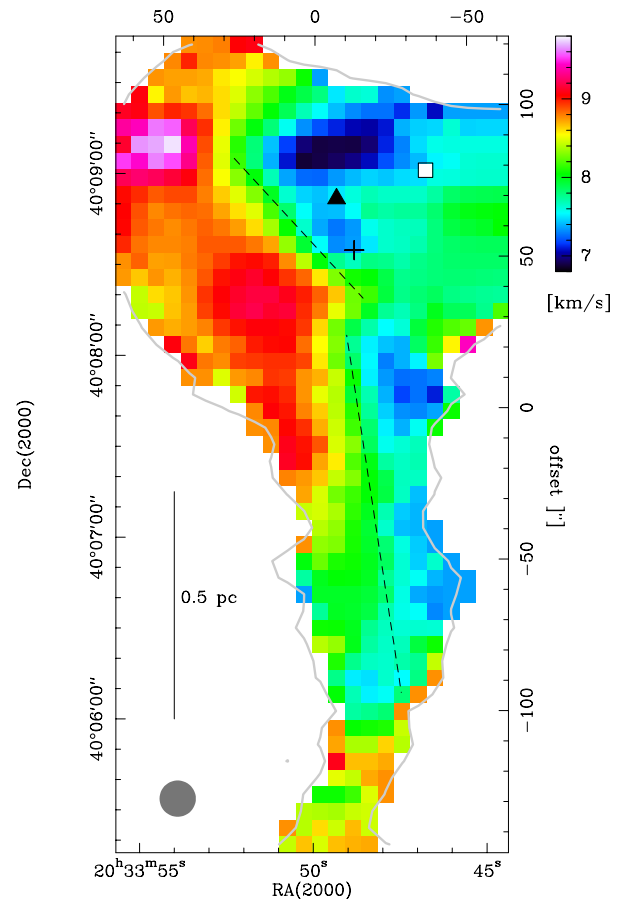


Fig. 8. Velocity map (first moment) of the [C II] emission, showing possible patterns of counter-clockwise rotation with the approximate axes indicated with dashed lines. The centre position (0,0) is at $\text{RA}(2000)=20^{\text{h}}33^{\text{m}}49.95$, $\text{Dec}(2000)=40^{\circ}07'42.75''$. The [C II] beam is indicated in the lower left corner. We note that the axes for the globule head, where most of the mass resides, and the tail have not the same inclinations, and the velocity difference is larger for the head (~ 9.5 to $\sim 6.9 \text{ km s}^{-1}$) than for the tail (~ 8.3 to $\sim 7.4 \text{ km s}^{-1}$). The grey contour outlines the 2 K km s^{-1} contour level of [C II] emission, the symbols are the same as in Fig. 4.

in [C II] before. The globule head shows a possible rotation feature with an inclined north-south axis, similar what was seen in Schneider et al. (2012). The globule tail also shows a possible rotation, but the axis is less inclined and the velocity difference is smaller. The rotation is clock-wise around an axis located between the blue and red part of the tail if we view the globule from above.

Possible rotation features in pillars were observed before (Gahm et al. 2006; Sofue 2020). Gahm et al. (2006) proposed for 'elephant trunks' in several sources observed in CO lines that rotation can be provoked by the formation of compressed magnetic filaments that were present in the parent molecular cloud and are now impacted by the expanding H II region. They developed a double helix model in which a pillar rotates as a solid body with the same angular speed along the major axis. This picture would be consistent with the observations for our globule. In this case, it is possible that the globule started as a pillar (proposed in Schneider et al. (2016)), which was linked to the bulk emission of the molecular cloud and had the same velocity. After the pillar detaches from the cloud, it becomes a globule

that floats freely into space but still carries the initial momentum of the pillar. Simulations (Tremblin et al. 2012b) predict that pillars and globules in the same close environment have a velocity difference of typically a few km s^{-1} . This applies also to our globule, as shown in Schneider et al. (2012). Other models of UV radiation impacting a turbulent cloud (Gritschneider et al. 2009) display a slightly different picture. The UV-radiation clears out and pushes away the low-density material of the cloud but leaves dense structures, such as pillars (see their Fig. 1). The extent to which magnetic fields and the impact of the external UV-radiation can also influence the velocity field seen in [C II] is not clear and this area requires further investigation.

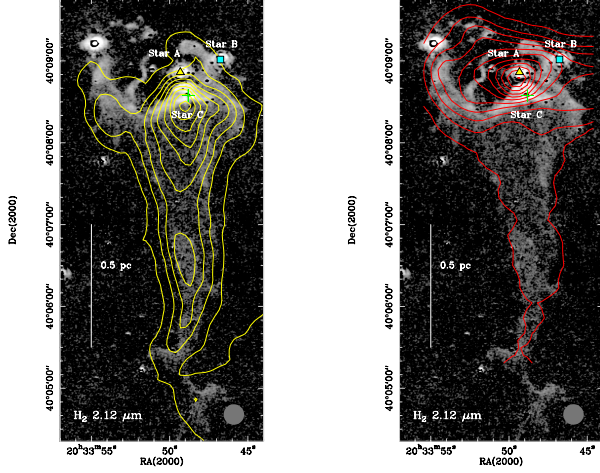


Fig. 9. Continuum subtracted narrow-band image that contains the H_2 1-0 S(1) ro-vibrational line at $2.122 \mu\text{m}$ (Djupvik et al. 2017) at $\sim 2''$ resolution with contours of velocity-integrated ^{12}CO 3→2 emission (yellow, left panel) and velocity-integrated [C II] emission (red, right panel), both at $15''$ resolution, overlaid. The CO contours go from 1 to 13 by 1.5 K km s^{-1} and the [C II] contours go from 5 to 155 by 15 K km s^{-1} . The embedded stars A, B, and C are indicated.

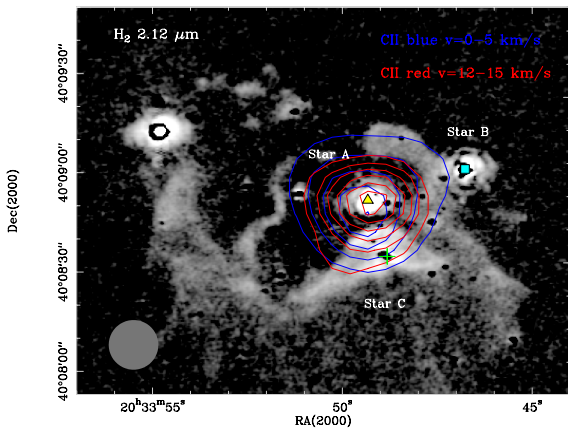


Fig. 10. Map of H_2 $2.12 \mu\text{m}$ emission (Djupvik et al. 2017) with contours of [C II] outflow emission. The blue velocity range of the [C II] line ranges from 0 to 5 km s^{-1} , contours go from 10 to 50 by 10 K km s^{-1} . The red velocity range is 12 to 15 km s^{-1} and contours go from 3 to 13 by 2 K km s^{-1} . The embedded stars and the [C II] beam size are indicated.

Table 5. Line fluxes and ratios for one position in the globule head.

Instrument	Species	$I(\Theta=20'')$	$I(\Theta=20'')$	Ratio
		[K km s^{-1}]	[$\text{erg s}^{-1} \text{ cm}^{-2} \text{ sr}^{-1}$]	
HIFI	[C II] 158 μm	153.5	1.08E-03	-
PACS	[O I] 145 μm	25.5	2.29E-04	-
upGREAT	[O I] 63 μm	6.3	6.85E-04	-
SPIRE	[C I] 2-1	7.4	4.04E-06	-
SPIRE	[C I] 1-0	10.2	1.25E-06	-
upGREAT	^{12}CO 16→15	1.1	7.03E-06	-
SPIRE	^{12}CO 13→12	9.3	3.19E-05	-
SPIRE	^{12}CO 12→11	14.9	4.02E-05	-
SPIRE	^{12}CO 11→10	20.5	4.27E-05	-
SPIRE	^{12}CO 10→9	26.4	4.13E-05	-
SPIRE	^{12}CO 9→8	31.7	3.62E-05	-
SPIRE	^{12}CO 8→7	45.1	3.62E-05	-
SPIRE	^{12}CO 7→6	51.3	2.76E-05	-
SPIRE	^{12}CO 6→5	68.2	2.31E-05	-
SPIRE	^{12}CO 5→4	91.8	1.80E-05	-
SPIRE	^{12}CO 4→3	104.6	1.05E-05	-
SPIRE	^{13}CO 9→8	2.6	2.61E-06	-
SPIRE	^{13}CO 8→7	5.5	3.86E-06	-
SPIRE	^{13}CO 7→6	9.0	4.24E-06	-
SPIRE	^{13}CO 6→5	11.1	3.30E-06	-
SPIRE	^{13}CO 5→4	19.9	3.41E-06	-
SPIRE	[C I] 2-1/1-0	-	-	3.23
SPIRE	^{12}CO 8-7/7-6	-	-	1.19
SPIRE	^{12}CO 6-5/5-4	-	-	1.71
SPIRE	^{12}CO 5-4/4-3	-	-	1.94
SPIRE	^{13}CO 8-7/7-6	-	-	0.91
SPIRE	^{13}CO 6-5/5-4	-	-	0.97

Notes. The fluxes are given in $\text{erg s}^{-1} \text{ cm}^{-2} \text{ sr}^{-1}$, the ratios are determined from these fluxes for the SPIRE central pixel in the globule head ($\text{RA}(2000)=20^{\text{h}}33^{\text{m}}50^{\text{s}}$, $\text{Dec}(2000)=40^{\circ}08'36''$). All data points have the same angular resolution of $20''$. The absolute error for the SPIRE data for the [C I] lines and CO $J \leq 8$ is $2.5\text{--}3.1\text{E}07 \text{ erg s}^{-1} \text{ cm}^{-2} \text{ sr}^{-1}$ and for $J > 8$ $\sim 9\text{E}07 \text{ erg s}^{-1} \text{ cm}^{-2}$. The low- and mid-J CO data have a resolution of $\sim 30\text{--}40''$ so that we only use line ratios.

4.4. Comparison to H_2 emission and small-scale dynamics of [C II] emission

Figure 9 shows how the emission distributions of cool molecular gas (traced by CO) and warm PDR gas (traced by [C II]) compare to the narrow-band imaging of the H_2 1-0 S(1) at $2.122 \mu\text{m}$. This line is excited either by shocks, driven by stellar winds, but can also be associated with dense PDRs. A large opening towards the north-east becomes obvious in the H_2 and CO 3→2 map and suggests that the internal H II region breaks out of the globule. The deficit of molecular gas is also clearly seen in the *Herschel* column density map in Fig. 3. In contrast, the peak in column density seen in Fig. 3 corresponds also to peak emission in CO and H_2 , and Star C is centred on this dense clump. Interestingly, the [C II] emission shows no decline in the north-eastern corner of the globule (right panel in Fig. 9) and the emission peak is clearly centred on Star A. In fact, we observe high-velocity blue- and red-shifted emission in [C II], shown in Fig. 10, suggesting an outflow oriented along the line-of-sight of the observer. The outflow is very collimated and could thus originate from a young stellar object (YSO) (the [C II] beam is $15''$ so that the emission is beam diluted). It is unlikely that this very localised outflow interacts with the external UV field. The red wing (velocities

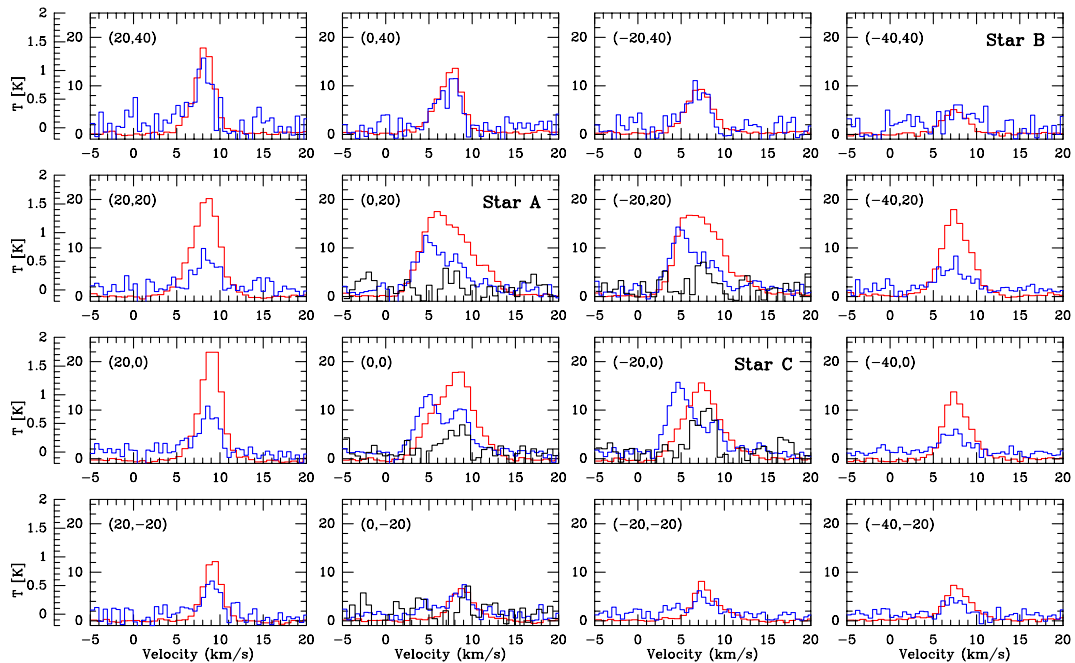


Fig. 11. Spectral maps of the [O I] 63 μm line (blue), the [C II] 158 μm line (red) and the CO 16 \rightarrow 15 line (black) of the globule head in the velocity range -5 to 20 km s^{-1} . The leftmost main beam brightness temperature scale ranges from -0.2 to 2 K and is valid for [O I] and CO 16 \rightarrow 15. The temperature scales at each panel are valid for [C II]. All data are smoothed to an angular resolution of $20''$ and sampled on a grid of $20''$ in order to increase the S/N. However, the CO 16 \rightarrow 15 line was not observed at all positions (Sect. 2) so that we only plot the few spectra with observed emission above the 5σ level. The velocity resolution is 0.5 , 0.7 , and 0.6 km s^{-1} for [O I], [C II], and CO 16 \rightarrow 15, respectively. The map centre position is $\text{RA}(2000)=20^{\text{h}}33^{\text{m}}50^{\text{s}}$, $\text{Dec}(2000)=40^{\circ}08'36''$. The approximate locations of the star systems are indicated.

$>12 \text{ km s}^{-1}$) is fully visible in the [C II] spectra taken around the position of Star A and displayed in Fig. 11. There is no high-velocity emission detected in CO 16 \rightarrow 15 and only a very weak velocity component in [O I] 63 μm around 12 km s^{-1} .

In Djupvik et al. (2017), we found that Star A has two components of which one is an early B-type star, a Herbig Be star. These objects are intermediate-mass pre-main-sequence stars and are divided into three categories (Fuente et al. 2002): The youngest ($\sim 0.1 \text{ Myr}$) Type I stars are embedded in a dense molecular clump and have associated bipolar outflows that are detected in CO. Type II stars are also associated to molecular material, but not immersed in a dense clump, their ages are between a few 0.1 to a few Myr . Type III stars (typical age $>1 \text{ Myr}$) have fully dispersed the surrounding material and created a cavity inside the molecular cloud. In addition, Diaz et al. (1998) showed that only stars with spectral type earlier than B5 can create significant PDRs. Our observations are, thus, fit best with an Herbig Be Type III star since we observe that the star is located in a cavity and not associated with a dense clump, that there is no CO outflow, but high-velocity [C II] emission, tracing the PDR surfaces of the inner cavity walls, namely, the interface between the H II region and the molecular gas. This sort of [C II] dynamics was also observed - and interpreted in a similar way - for the bipolar nebula S106 (Schneider et al. 2018). We note that we exclude shock excitation as a significant origin for the outflow because firstly, [C II] is not a good shock tracer and its origin is mostly PDRs, and secondly, the [O I] 63 μm line does not show prominent high-velocity wings, which would be the case if there were shocks.

It is out of the scope of this paper to go into more detail what is the driving source for the [C II] outflow, but we note that it must be associated with the Herbig Be star. In the literature on Herbig Ae and Be stars, accretion and outflow signatures

were detected (Cauley & Johns-Krull 2014; Moura et al. 2020; Rodriguez et al. 2014), and stellar winds are commonly promoted as the most likely outflow mechanism, although magneto-centrifugally driven outflows from the star-disk interaction region can also occur. Higher angular resolution cm-observations and spectroscopy of lines from the stellar atmosphere of the star may help to investigate in more detail the accretion and outflow properties of the source.

In any case, we confirm the conclusion from Djupvik et al. (2017) that the emission distribution of H_2 indicates that the sources of ionisation are the B stars of the embedded aggregate, rather than the external UV field caused by the O-stars of Cyg OB2. We note that another line of evidence in Djupvik et al. (2017) showed that the visible spectrum of the H II region is that of a soft ionising radiation, typical of an early-B star. In Sec. 5.1, we will give further evidence for this proposal by modelling the observed FIR lines.

4.5. [O I] 63 μm and CO 16 \rightarrow 15 line mapping with upGREAT/SOFIA and PACS/SPIRE spectroscopic maps

Figure 11 shows a spectra map of the globule head observed in the [O I] 63 μm , the [C II] 158 μm and CO 16 \rightarrow 15 lines with upGREAT on SOFIA. The [O I] spectra also show that there are several velocity components and not a single Gaussian line profile but comparing to the [C II] and CO 16 \rightarrow 15 emission reveals that the line profile is moreover due to self-absorption. The CO 16 \rightarrow 15 line peaks at a velocity of $\sim 9 \text{ km s}^{-1}$ where there is a dip in [O I] emission and where the [C II] line also reveals a decrease. This indicates that the [C II] line can also be slightly self-absorbed at the peak positions though this is difficult to tell because of the broad red wings due to the [C II] outflow. The velocity component at $\sim 9 \text{ km s}^{-1}$ seen in [O I], CO 16 \rightarrow 15 and

Table 6. Line fluxes and ratios for one position in the globule tail.

Instrument	Species	$I(\Theta=40'')$ [K km s ⁻¹]	$I(\Theta=40'')$ [erg s ⁻¹ cm ⁻² sr ⁻¹]	Ratio
HIFI	[C II] 158 μ m	10.0	7.03E-05	-
SPIRE	¹² CO 11→10	0.78	1.60E-06	-
SPIRE	¹² CO 10→9	1.46	2.29E-06	-
SPIRE	¹² CO 9→8	4.38	5.00E-06	-
SPIRE	¹² CO 8→7	6.99	5.61E-06	-
SPIRE	¹² CO 7→6	12.50	6.72E-06	-
SPIRE	¹² CO 6→5	18.81	6.37E-06	-
SPIRE	¹² CO 5→4	29.23	5.73E-06	-
SPIRE	¹² CO 4→3	31.68	3.18E-06	-
SPIRE	¹³ CO 8→7	0.96	0.67E-06	-
SPIRE	¹³ CO 7→6	1.25	0.59E-06	-
SPIRE	¹³ CO 6→5	3.51	1.04E-06	-
SPIRE	¹³ CO 5→4	7.53	1.29E-06	-
SPIRE	[C I] 2-1	4.66	2.53E-06	-
SPIRE	[C I] 1-0	7.38	9.01E-07	-
SPIRE	[C I] 2-1/1-0	-	-	2.81
SPIRE	¹² CO 8-7/7-6	-	-	0.83
SPIRE	¹² CO 6-5/5-4	-	-	1.11
SPIRE	¹² CO 5-4/4-3	-	-	1.80
SPIRE	¹³ CO 8-7/7-6	-	-	1.13
SPIRE	¹³ CO 6-5/5-4	-	-	0.81

Notes. The fluxes are given in erg s⁻¹ cm⁻² sr⁻¹, the ratios are determined from these fluxes for the SPIRE central pixel in the globule tail (RA(2000)=20^h33^m49^s, Dec(2000)=40°06′40.2″). All data points have the same angular resolution of 40″. The absolute error for the SPIRE data varies between 2.5 and 3.1E07 erg s⁻¹ cm⁻² sr⁻¹. Note that there are less observations for the globule tail position compared to the head and the lines are weaker.

[C II] is mostly associated with the dynamics caused by the impact of the Herbig Be star on the surrounding molecular cloud (see Sec. 4.4).

The SOFIA data confirm the PACS [O I] 63 μ m map (Fig. A.1 in the Appendix), indicating that the velocity integrated [O I] emission is very localised. Interestingly, the peak [O I] emission is not found at the position of Star A (as is the case for [C II] emission) or at the position of Star C. Moreover, it peaks in between the two stars and correlates partly with the extended clump seen in H₂ emission (Fig. 10). Furthermore, we note that the [N II] lines at 122 μ m and 205 μ m (Figs. A.1 and A.2 in the appendix), best tracing the H II region, have their emission peak close to Star A, further north than the [O I] and CO 16→15 peaks.

5. Discussion

Summarising the observations presented in Sec. 4, it becomes obvious that we detect different gas components in the globule. The [C II] emission revealed widespread, extended emission in the globule head and tail at bulk velocities (~ 8 km s⁻¹). The carbon in this component is probably mostly excited by the external Cyg OB2 cluster that impacts the globule from a north-western direction. Cosmic-ray (CR) excitation can also contribute, but the UV-field at the location of the globule is still a few 100 G₀ and thus dominates over CRs. The tail is exclusively externally heated, but the globule head contains intermediate stars that created a cavity with an internal PDR surface that also emits in [C II] and in other typical cooling lines (high-J CO, [O I]). Red-

and blue-shifted high-velocity [C II] outflow emission is caused by the Herbig Be star A in the globule head. In the following, we will disentangle the different gas components and determine their physical properties in the globule head and tail, using PDR modelling.

5.1. PDR modelling

We compare the observed line intensities and ratios with predictions from the KOSMA- τ PDR model (Röllig et al. 2006, 2013). This model is able to compute line and continuum emission arising from spherical clouds as well as for clumpy PDR ensembles (Cubick et al. 2008; Andree-Labsch et al. 2017). The full model parameters are summarised in Table B.1 in Appendix B, we here vary the most important variables that are density n [cm⁻³], mass M [M_⊙], and FUV field strength χ in units of the Draine field. KOSMA- τ can model single spherical clumps (non-clumpy PDR model) and ensembles of clumps (clumpy PDR model), according to a clump-mass distribution law (for details see Cubick et al. 2008; Andree-Labsch et al. 2017). Because the model has a finite mass and the volume of different chemical species (and thus the corresponding angular filling factors) are self-consistently considered, KOSMA- τ is able to compute absolute intensities that are directly comparable to observations. Summarising, we apply the following modeling strategy:

We modelled a single position for the globule head and tail, respectively. The head position is at RA(2000)=20^h33^m50^s, Dec(2000)=40°8′36″. This is the centre position of the SPIRE map of the globule head and indicated in Figs. 4 and A.1. It is not a peak emission position for many lines, but we have the largest data set for this point. For the tail, the data set is even smaller and contains mostly SPIRE lines. We take the central position of the map at RA(2000)=20^h33^m49^s, Dec(2000)=40°06′40.2″.

In order to account for the different beam sizes, the velocity integrated line intensities of [C II] 158 μ m, [O I] 63 μ m and 145 μ m, CO 16→15, CO 13→12, CO 12→11, CO 11→10, CO 10→9, CO 9→8, and ¹³CO 9→8, were all smoothed to a common angular resolution of 20″ for the globule head and 40″ for the tail. A distance of 1.4 kpc is adopted.

The CO transitions lower than J=8→7 and the two [C I] transitions have a larger beam size of typically 30″–45″ (principally the SPIRE observations). For the globule head, we thus compared the line ratios (CO 8→7/7→6, CO 6→5/5→4, ¹³CO 8→7/7→6, ¹³CO 6→5/5→4, and [C I] 2→1/1→0) to cancel out beam size effects to the first order. For the globule tail, we used absolute intensities because all line intensities are smoothed to 40″, but give the ratios in Table 6 for information. The best-fitting model parameters are summarised in Table 7.

5.2. Clumpy versus non-clumpy models for the globule head

We showed in the previous sections that the globule head is subject to an internal FUV field produced by the embedded star system and an external FUV field produced by the Cyg OB2 association. The observed line intensities are thus the superposition of the two PDRs and consequently we assume a two-component PDR model. Two non-clumpy PDR components are ruled out due to the strong emission for the high-J CO ($J > 10$) transitions which requires larger amounts of hot (surface) CO than can be explained in non-clumpy models. Similarly, two clumpy PDR components are unable to explain the observed high levels of [C II] and [O I] emission. We thus set up a two-component model that consists of a non-clumpy external PDR component

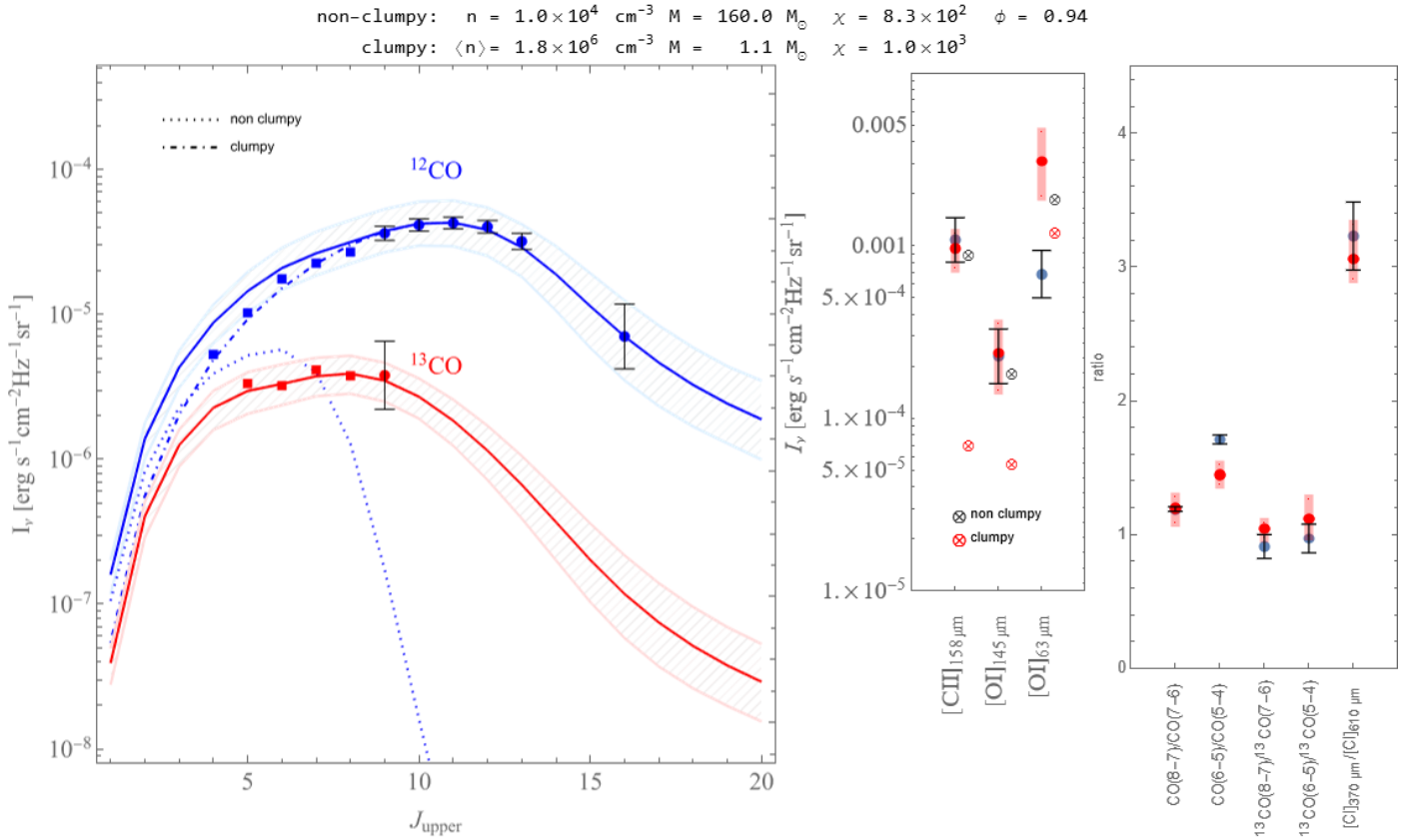


Fig. 12. PDR model results of the two-component globule model. The left panel shows the ^{12}CO (blue lines) and ^{13}CO (red lines) model SLED (spectral line energy distribution) together with the observed data (blue for ^{12}CO and red for ^{13}CO , respectively). We note that data points without error bars are excluded from the fit but are shown as a consistency check. The non-clumpy and clumpy contribution to the total SLED are displayed with dotted and dash-dotted lines, respectively. The hatched areas around the SLED's indicate the model sensitivity to 20% variations of the model parameters. The centre panel shows the fine-structure line data. We note that the $[\text{OI}] 63\mu\text{m}$ line was excluded from the fit. The blue dots (with error bars) are the observations and the red dots are the model derived values with the red bands indicating the model response to 20% parameter variations. For each line intensity, we show for information their contribution from the non-clumpy and clumpy components with black and red crossed circles, respectively (with a slight offset to the right for easier reading). The right right panel displays the behavior of the various line ratios with the same coding.

Table 7. Summary of the best-fit models for the globule head and tail positions.

parameter	value	description
globule head		
non-clumpy component		
n_{n-c}	$1.0 \times 10^4 \text{ cm}^{-3}$	total gas density
M_{n-c}	$160 M_{\odot}$	total clump mass
χ_{n-c}	$830 \chi_{\text{Draine}}$	FUV field strength
ϕ	0.943	beam filling factor
clumpy component		
$\langle n_c \rangle$	$1.8 \times 10^6 \text{ cm}^{-3}$	mean ensemble gas density
M_c	$1.1 M_{\odot}$	ensemble mass
χ_c	$1.0 \times 10^3 \chi_{\text{Draine}}$	FUV field strength
globule tail		
n	$7.6 \times 10^4 \text{ cm}^{-3}$	total gas density
M	$70 M_{\odot}$	total clump mass
χ	$81 \chi_{\text{Draine}}$	FUV field strength
ϕ	0.3	beam filling factor

illuminated by the Cyg OB2 cluster and an internal clumpy PDR illuminated by the embedded stars (see Sect. 5.4). This scenario is the one we already proposed in the sections before for ex-

plaining the spatial and kinematic emission distributions of the FIR lines.

The external PDR (non-clumpy) corresponds to a single spherical clump with the surface density n_{n-c} , mass M_{n-c} , UV-field χ_{n-c} and considering a beam filling factor, ϕ . This model component corresponds to the yellow and gray spherical shells shown in Fig. 15.

The internal PDR (clumpy) corresponds to a clumpy PDR ensemble, with the ensemble averaged density clump density $\langle n_c \rangle$, mass M_c , UV field χ_c and a beam size of $20''$. This component is depicted as ensemble of golden clumps in Fig. 15.

In addition to these components, there is also the H II region cavity around star A (indicated in red in Fig. 15). This one is rather small ($\sim 15''$ - $20''$) as can be inferred from the extend of $[\text{N II}]$ emission (Fig. A.1) and from our UV-field estimate (Sect. 5.4). We did not model the H II region (using a different code since KOSMA- τ is not designed for that) to explain the $[\text{N II}]$ lines because this is out of the scope of this paper.

We numerically minimise the reduced chi-square function for the seven free parameters:

$$\chi^2 = \frac{1}{N_I + N_R - 7} \left(\sum_{i=1}^{N_I} p_i \frac{I_{\text{obs},i} - I_{\text{mod},i}}{\epsilon_{I,i}} + \sum_{i=1}^{N_R} p_i \frac{R_{\text{obs},i} - R_{\text{mod},i}}{\epsilon_{R,i}} \right), \quad (3)$$

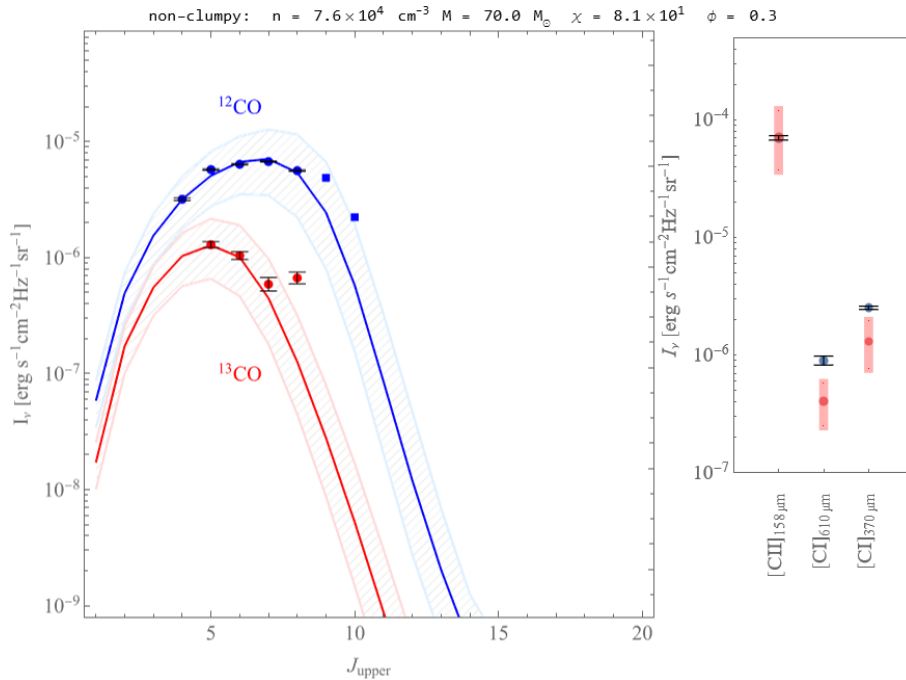


Fig. 13. PDR model results of the non-clumpy globule tail model. The left panel shows the ^{12}CO (blue points and line) and ^{13}CO (red points and line) model SLED (spectral line energy distribution). This is the best-fitting non-clumpy model. The colour-shaded areas give the range of models by varying all parameters by $\pm 20\%$. The right panel shows the observed (blue) and modelled (red) fine-structure line fluxes for this model, with the model variations indicated by the vertical red bands. Data points without error bars, namely, the two highest- J ^{12}CO lines $J=10\rightarrow 9$ and $9\rightarrow 8$, are excluded from the fit, but shown to provide further information.

summing over all N_I line transitions I and N_R line ratios R to be included. The error depends on the observed tracer, we used the absolute error for the SPIRE observations (see Tables 5 and 6), a 30% error for the PACS data, 20% for (up)-GREAT/SOFIA and 10% for HIFI observations (see Sec. 2.6). We introduce a penalty factor, p_i , to allow for weaker or stronger weighting of individual transitions or ratios in the numeric fit. χ^2 is minimised in logarithmic space using the Nelder-Mead method assuming a shrink and contract ratio of 0.85, and a reflect a ratio of 3 using the software *Mathematica* (Mathematica Ver.12 2020).

The best fitting model parameters, assuming $p_i = 1$ for all i with the exception $p_{(16-15)} = 1000$, are $n_{n-c} = 1.0 \times 10^4 \text{ cm}^{-3}$, $M_{n-c} = 160 M_{\odot}$, $\chi_{n-c} = 830$, $\phi = 0.94$, and $\langle n_c \rangle = 1.8 \times 10^6 \text{ cm}^{-3}$, $M_c = 1.1 M_{\odot}$, $\chi_c = 10^3$ with a $\chi^2 = 5.8$. To assess the sensitivity of the result to the model parameters we varied all parameters by 20% (ϕ was varied by ± 0.1) and present the resulting intensity variations as coloured bands around the best fit result. Across all intensities and ratios a 20% parameter variation changes the model intensities and intensity ratios by 46 – 110%. The total model mass of $160 M_{\odot}$ is a good fit to the mass determined from the dust ($166 M_{\odot}$), while the FUV field strengths are somewhat different from complementary estimates. These differences are discussed in Sect. 5.4.

Overall, the model intensity fit is very good with the exception of the $[\text{O I}] 63 \mu\text{m}$ line, where the model intensities are about a factor of 10 too high, while the $[\text{O I}] 145 \mu\text{m}$ line is well reproduced. The over-prediction of $[\text{O I}] 63 \mu\text{m}$ intensity is a notorious problem that we attribute to an absorbing foreground layer (between the clumpy PDR and the observer), resulting in a significant optical depth along the line of sight. This is in agreement with recent SOFIA observations of star-forming regions where the $[\text{O I}] 63 \mu\text{m}$ line was found to be heavily affected by foreground absorption while the upper $[\text{O I}] 145 \mu\text{m}$ line is mostly unaffected (Schneider et al. 2018; Guevara et al. 2020). Figure 11

also shows that the $[\text{O I}] 63 \mu\text{m}$ line arising from the PDR of the globule head suffers from significant self-absorption. A factor of ~ 10 in missing intensity is fully reasonable, although we cannot estimate the exact value, which is the reason for excluding the line from the numerical fit.

In order to assess the relative contribution of the clumpy and the non-clumpy component we separately plot the predicted emission in the left panel of Fig. 12. The three fine-structure lines show a different fraction of their emission coming from either component, resulting in a relatively sensitive probe to the degree of clumpiness in the region. We note that the $[\text{C II}]$ emission receives a large contribution from the non-clumpy PDR. This points towards a scenario that the $[\text{C II}]$ emission at velocities of the bulk emission of the globule is mostly caused by the external excitation from Cyg OB2. This is what we also concluded from the extended emission distribution seen in the $[\text{C II}]$ maps. We note that ionised carbon is probably well mixed within the non-clumpy PDR component – and not only a thin external surface layer because we detect the rotation of the globule in $[\text{C II}]$. It is unlikely that it is only the external surface layer that is rotating. In addition, we presume that there is little $[\text{C II}]$ emission coming from the ionised phase because the PDR model alone already well explains the observed intensities. However, we only modelled one point and cannot thus conclude over the full globule head.

5.3. Non-clumpy model for the globule tail

The position we model in the globule tail (Fig. 4) is a more quiescent location than the one in the globule head since there are no internal sources and excitation happens only externally via the OB-cluster and by cosmic rays. We performed the fit with data smoothed to a larger beam size ($40''$) and tested again various models and found that a non-clumpy model with a single model

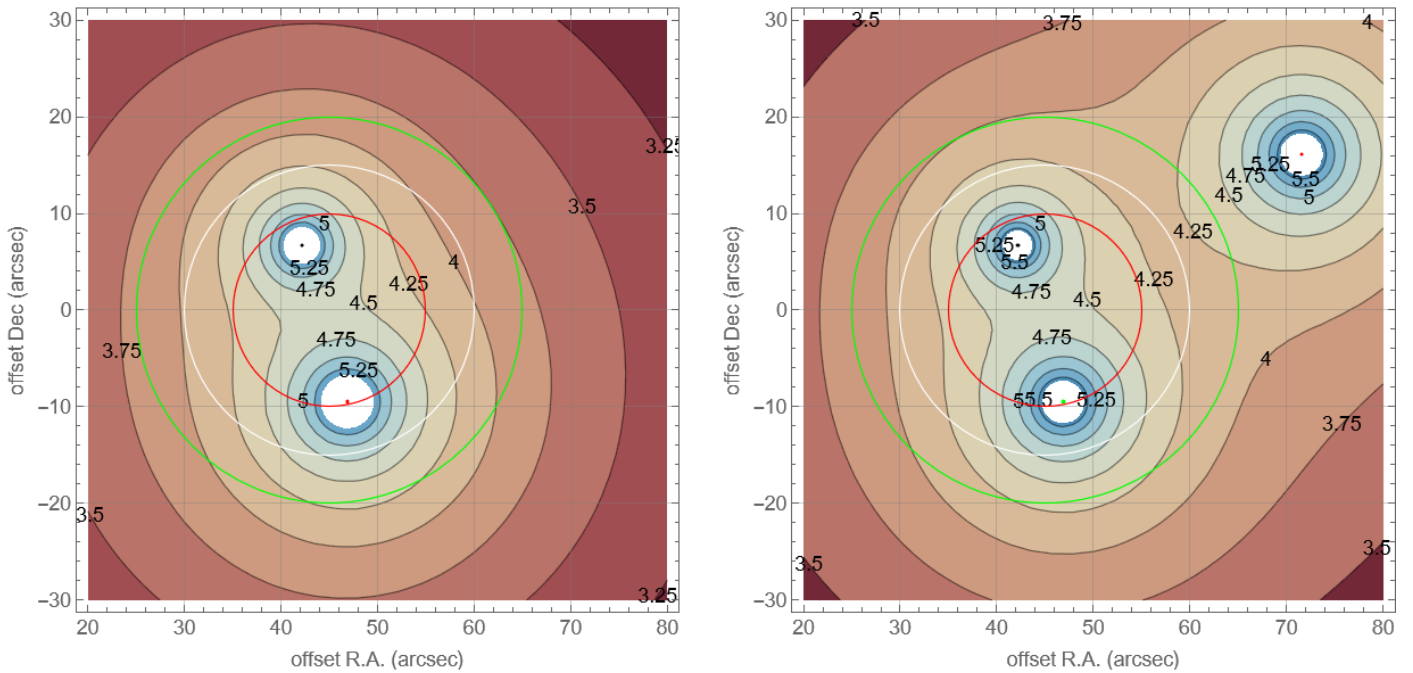


Fig. 14. FUV estimate for the globule. The three main stars A,B, and C are assumed to reside in the same plane on the sky. Spatial variations are shown in units of arcsec. The values of the contours are $\log \chi$ where the Draine field χ has been computed from pure geometrical dilution. The two panels show χ excluding (left) and including (right) Star B. For information on the size scale, we plot three circles with radii of 10'' (red), 15'' (white), and 20'' (green) around a central position between Star A and C.

component gives the best fitting results. These are displayed in Fig. 13 and show the SLEDs for the globule tail position with the observed CO line fluxes in ^{12}CO and ^{13}CO . The ^{12}CO 10 \rightarrow 9 and 9 \rightarrow 8 and the ^{13}CO 8 \rightarrow 7 transitions have to be treated with care because the lines are weak and just above the noise level. The mass of the model was fixed to 70 M_{\odot} , following the value determined from the dust column density (Sec. 3). All model parameters were varied and the colour-shaded areas in the left panel and coloured band in the right panel of Fig. 13 show how much the model intensities change. The illumination of the tail is assumed to be one-side only. The right panel displays the observational (blue) and model (red) fluxes for the [C II] and [C I] lines. Overall, a model with a UV field of around $\chi = 80$ (corresponding to 137 G_{\odot}) and a density of $\sim 8 \cdot 10^4 \text{ cm}^{-3}$ with a filling factor of 0.3 fits our observations ($\chi^2 = 1.9$). The low model UV field is interesting, it is the lower limit from what was determined from the census of Cyg OB2 stars or the *Herschel* flux. Nevertheless, the non-clumpy fit for the globule tail is less convincing compared to the globule head model. The [C II] model intensities match the observed value and the ^{12}CO lines are well reproduced up to 8 \rightarrow 7. The two lowest ^{13}CO lines fit the observations well, the upper lines are underestimated as well as the higher-J ^{12}CO lines. Both [C I] fine-structure lines are significantly underestimated. The fit returned a filling factor of 0.3, namely, only 1/3 of the tail at the assumed position is supposedly illuminated by FUV. Comparing the [C II] contours in Fig. 4 with the beam size at the tail position would suggest a significantly larger filling of about 2/3. This emphasises the limits of the non-clumpy, single-component model that we applied. The next step could be a multi-component model, but this would require more data, for instance, the [O I] fine-structure lines. In addition, the high-J ^{13}CO lines show a non-monotonous trend after the SLED peak, which is difficult to explain in a simple model.

5.4. UV field estimate for the globule head

We assume that the FUV field affecting the gas in the globule has two components. Firstly, an external radiation field, created by the massive stars of the Cyg OB2 association, and secondly, an internal radiation field created by the YSO embedded in the globule. In Schneider et al. (2012) and Schneider et al. (2016), we already presented an estimation of the FUV field based on the number of O-stars in Cyg OB2 and on the *Herschel* fluxes at 70 and 160 μm . We arrived to a value of $G_{\odot} \approx 313$ ($\chi \approx 183$), considering 50 O-stars at the position of the globule at a distance of ~ 30 pc from Cyg OB2. These are upper limits since no extinction but only $1/r^2$ distance dilution was considered. We also did not take into account possible shadowing effects from the globule's head. The number of O-stars in Cyg OB2, however, is uncertain and estimates range between ~ 50 (Comerón et al. 2002; Wright et al. 2015) and ~ 120 (Knödlseeder 2000). The FUV field derived from the *Herschel* fluxes (right panel in Fig. 3) is ~ 150 -200 G_{\odot} for the globule tail, where we can assume that the illumination is only caused by the external radiation field. In summary, a value of 150-300 G_{\odot} (88 -176 χ) is probably a reasonable assumption for the total external radiation field impacting the globule. However, the field strength necessary to explain the non-clumpy PDR emission is about two to three times stronger than that. Possible reasons for this discrepancy could come from a significantly higher number of OB stars in the cluster, as suggested by Knödlseeder (2000). This would still be in conflict with the FUV estimates for the tail and it is unclear whether those can be explained by geometrical effects, for instance shielding or shadowing by the globule head. Alternative explanations for the higher FUV illuminating the external PDR could be an additional, possibly closer source such as the YSO B (see discussion below) or a much stronger fragmentation of the molecular gas in

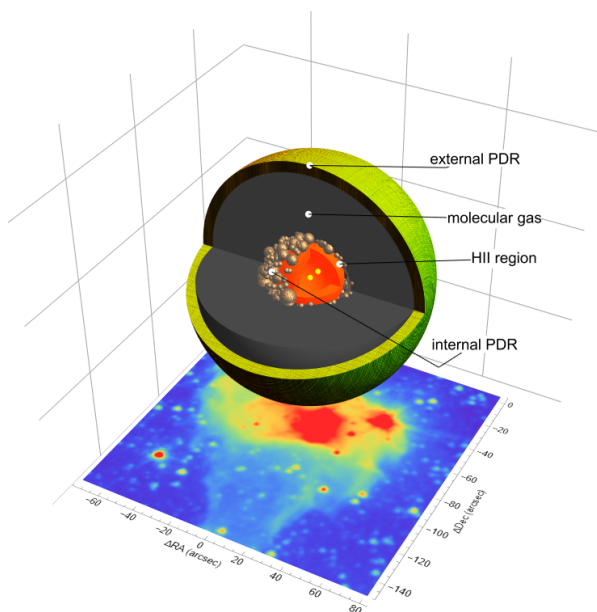


Fig. 15. Model geometry of the observed globule hosting two embedded YSO and an internal embedded cavity/H II region. The relative sizes of the individual shells are not shown to scale. The external non-clumpy PDR is shown as yellow outer shell, the internal, clumpy PDR is shown as golden clump ensembles between the embedded H II region and the molecular cloud shown as gray spherical shell. The image projected on the bottom plane is *Spitzer* 8 μ m emission (for orientation, the flux values are not of interest here). The offsets are given in arcsec referring to the position RA(2000)=20^h33^m49.95^s, Dec(2000)=40°07′42.75″. UV-radiation impacts externally via the Cyg OB2 cluster and internally via the YSOs. The cavity radius is approximately 15″–20″, determined from modelling and consistent with the region of brightest IR emission.

the head that allows the internally generated FUV to escape and also affect the external PDR.

Inside the globule head, the internal sources produce an internal Strömgren sphere embedded in the globule and illuminate the inner surface of the remaining spherical shell. Here, we estimate the strength for this internal radiation field for comparison and as a constraint for the PDR model. The FUV field of the YSOs is dominated by the internal sources, named Star A, B, and C in Djupvik et al. (2017) and we compute the FUV intensity by assuming stellar black-body emission with $T_{\text{eff}} = 22600, 26200, 26200$ K and stellar luminosities $\log L = 3.72, 4.04, 4.04$, respectively, integrating over the FUV range from 910 to 3000 Å. The flux is diluted with $1/r^2$ and superposed in Fig. 14. Any additional attenuation, for instance, by dust is neglected, hence the result is an upper limit to the FUV field strength. Star B is slightly offset with regard to the H II region and the peaks of [C II] emission, so it is not clear whether this YSO is still embedded in the globule or whether it only appears related due to projection effects. However, the contribution of Star B to the radiation field close to our model position is relatively weak due to the larger distance. We thus assume that the internal FUV field is created by Stars A and C only. The PDR model fit gives a radiation field $\chi_c \sim 1000$ for the clumpy component. A comparison with Fig. 14 shows that the FUV field estimated from the census of the stars and assuming no extinction is higher, typically a factor of 2–3. On the other hand, the FUV field from the *Herschel* fluxes is $\chi \sim 2500$ in a 20″ beam at the peak position and

$\chi \sim 1500$ at the position where we perform the PDR modelling⁴. These values are in agreement with the PDR model estimates of the total FUV field (external and internal) which both contribute to the total continuum flux. The FUV derived from the *Herschel* fluxes and our model results differs from the census of the embedded stars. This cannot be explained via the dust attenuation of the FUV because any significant amount of dust in the H II region cavity that absorbs UV photons would still contribute to the IR continuum emission. The H II region cavity has a radius of $\sim 15''$ – $20''$, which is consistent with the extent of the area of brightest IR and H₂ and Br _{γ} emission (Figs. 2 and 7 in Djupvik et al. (2017)). A significantly larger cavity and, therefore, a lower FUV at the clumpy, internal PDR is unlikely. Most likely, our estimate of the FUV brightness of the embedded YSOs is too high due to lower T_{eff} and $\log L$.

5.5. Discussion of the model results

From the previous sections, we can see that the observed emission requires at least two PDR components: a non-clumpy, high mass component with a FUV illumination of $\chi_{n-c} \approx 850$, and a less massive clumpy PDR component that is about two orders of magnitude denser and requires a stronger FUV illumination of $\chi_c \approx 1000$. Given the geometrical constraints of the source, we propose the scenario outlined in Fig. 15. The embedded YSOs are creating a cavity/H II region embedded in the globule head. The inner surface of the remaining shell is compressed by the expanding H II region and possibly fragments into clumps, and is heated by the strong radiation of the YSOs.

The external surface of the globule is irradiated by the ambient FUV field and emits as a spherical (non-clumpy) PDR at a density of $\sim 10^4$ cm⁻³. The non-clumpy PDR component has a clump radius of $\sim 60''$, which is consistent with the observed extended FIR line emission of [C II] that traces mostly the outer PDR layer. Other lines with critical densities around 10^4 cm⁻³ and excitation temperatures around 50–100 K are the [C I] 2→1 and 1→0 lines and the mid-J CO lines. Their spatial emission distribution is also more extended than the emission lines of tracers that require higher densities and temperatures (such as the [O I] lines and the high-J CO lines, see Figs. A.1 and A.2). The latter have their origin in the PDR created at the internal surface of the cavity, which is clumpy and dense ($\sim 2 \times 10^6$ cm⁻³) and covers a relatively small volume due to its small mass. To test how realistic this scenario may be, we computed the thickness of the internal clumpy PDR layer because the clumpy PDR model fit returns the total PDR mass and volume ($V = 7.2 \times 10^{50}$ cm³) and this can be converted to a thickness as function of R_{cavity} . Accounting for irregularities and turbulent structures in the cavity surface, we can also apply a volume filling factor that describes how efficiently the clumpy PDR fill up the available volume.

Figure 16 shows how the PDR thickness varies as a function of R_{cavity} . We compare two volume filling scenarios. We find that the internal PDR layer is relatively thin with a thickness of $\approx 3 - 5 \times 10^{14}$ cm (0.9 – 1.6×10^{-4} pc) only. We used the radius of the H II region cavity of $\sim 15''$, corresponding to 0.14 pc, to derive the thickness. Geometrically, this is consistent with our picture of the internal PDR surface. However, the spherical shell picture would decrease the volume and mass of the remaining globule and is inconsistent with the assumption of a full spherical (non-clumpy) PDR. Naturally, this mostly affects the molec-

⁴ This estimation assumes that the dust in the PDR region and in the H II region cavity fully absorbs the emitted UV photons and re-emits in the FIR.

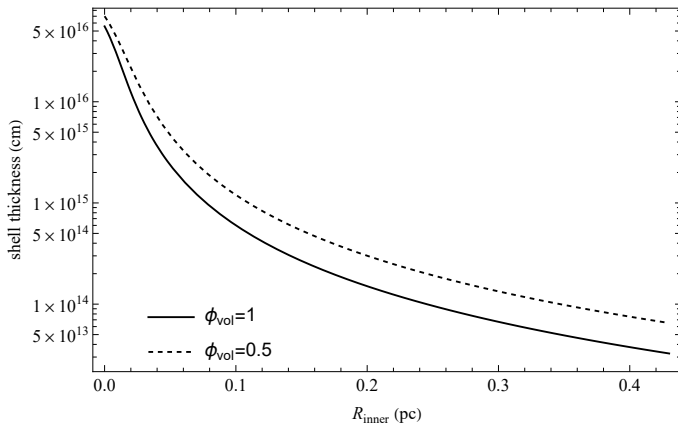


Fig. 16. Thickness of the internal PDR layer as function of cavity radius. Different lines correspond to variations in the volume filling factor of the ensemble.

ular cloud tracers. In our model, however, the non-clumpy PDR contributes mostly to the $[C II]$ emission and other surface tracers. We can, therefore, ignore this inconsistency at this point. We want to stress that the PDR model results were performed for all parameters independently. The proposed geometry also explains the over-predicted $[O I]$ $63 \mu m$ intensity. In the model fit we simply add the clumpy and non-clumpy contribution. Geometrically, however, the non-clumpy PDR shell around the clumpy PDR is optically thick against the $[O I]$ $63 \mu m$ line because the higher $[O I]$ levels are not excited. We conclude that the resulting model components very nicely fit into the proposed geometry scenario and agree with complementary constraints such as the strength of the internal FUV field, the globule mass, and the observed $[O I]$ self-absorption.

6. Conclusions and Summary

We presented new spectroscopic FIR data for the globule IRAS 20319+3958 in Cygnus X South, located at 1.4 kpc distance, obtained with HIFI, PACS, and SPIRE on *Herschel*, and with upGREAT on SOFIA. The observations include all important FIR cooling lines in the interstellar medium, namely, the $[C II]$ $158 \mu m$ line, the $[O I]$ $63 \mu m$ and $145 \mu m$ lines, the $[C I]$ $2 \rightarrow 1$, $1 \rightarrow 0$ lines, the mid- to high-J CO ladder ($16 \rightarrow 15$ down to $3 \rightarrow 2$), and the $[N II]$ lines at $205 \mu m$ and $122 \mu m$. These tracers cover a large range of excitation temperatures and densities.

The $[C II]$ line is the only FIR line that covers the full globule and is spectrally resolved. The kinematic $[C II]$ distribution revealed several features. Firstly, the $[C II]$ velocity map is consistent with rotation, that we attribute as a relic from the initial momentum the globule carried away while it was detaching from the molecular cloud. A comparison with the simulations would help in exploring this possibility. Secondly, we detected a rather collimated high-velocity blue- and red-shifted $[C II]$ outflow, associated with an embedded Herbig Be star. This star, together with two other systems of B-stars, is located inside the globule head and created an internal $H II$ region. The outflow is not visible in the $[O I]$ $63 \mu m$ line or in CO and we cannot discern the driving source, namely, the stellar wind of the Herbig Be star or the disk wind in case of an accretion disk.

We performed careful PDR modelling using the large observational data set of FIR lines (see above) for one position in the globule head and one in the tail. The objective was to determine

the physical properties of the PDR components that are responsible for the emission of the various cooling lines and to establish a geometrical model for the globule head.

The best-fitting model is one with an extended ($\sim 60''$ or ~ 0.4 pc), external non-clumpy PDR layer where most of the $[C II]$ emission originates. The UV radiation of the ~ 30 pc distant Cyg OB2 cluster estimated from the stellar census of a few hundred G_0 seems to be insufficient to account for the model FUV intensities of $G_0 \approx 1500$. A much larger stellar content of the OB cluster and/or additional possibly closer FUV sources may explain this discrepancy. The total mass from the PDR model is $\sim 160 M_\odot$, which corresponds well to the mass determined from dust ($166 M_\odot$), and an average density of 10^4 cm^{-3} . Between the shell and the $H II$ region cavity is a thin PDR layer (< 0.1 pc) that is clumpy, dense ($\sim 2 \times 10^6 \text{ cm}^{-3}$), but not very massive ($\sim 1 M_\odot$) and illuminated by the embedded YSOs that create a radiation field of $G_0 > 10^3$.

The tail position has no complex structure, the best fitting model is the one of a non-clumpy PDR with a mass of $\sim 70 M_\odot$, illuminated by an external UV field of $\sim 140 G_0$ which corresponds to the lower UV field limit derived from the census of the stars and the *Herschel* flux estimate and may hint at additional shadowing of the tail by the globule head.

With this study, we establish evidence in support of our proposal from Schneider et al. (2012) and Djupvik et al. (2017) that the globule is an example of a region where intermediate-mass stars form in isolation within a single dense clump. We also show that PDR modelling of many cooling lines and a consideration of a complex geometry allows us to successfully explain the observed intensities.

Acknowledgements. This work was supported by the Agence National de Recherche (ANR/France) and the Deutsche Forschungsgemeinschaft (DFG/Germany) through the project "GENESIS" (ANR-16-CE92-0035-01/DFG1591/2-1). N.S. acknowledges support from the BMBF, Projekt Number 50OR1714 (MOBS - Modellierung von Beobachtungsdaten SOFIA). This work is based on observations made with the NASA/DLR Stratospheric Observatory for Infrared Astronomy (SOFIA). SOFIA is jointly operated by the Universities Space Research Association, Inc. (USRA), under NASA contract NAS2-97001, and the Deutsches SOFIA Institut (DSI) under DLR contract 50 OK 0901 to the University of Stuttgart. This work was supported by the German *Deutsche Forschungsgemeinschaft*, DFG project number SFB 956.

GJW gratefully acknowledges the receipt of an Emeritus Fellowship from The Leverhulme Trust.

SPIRE has been developed by a consortium of institutes led by Cardiff University (UK) and including Univ. Lethbridge (Canada); NAOC (China); CEA, LAM (France); IFSI, Univ. Padua (Italy); IAC (Spain); Stockholm Observatory (Sweden); Imperial College London, RAL, UCL-MSSL, UKATC, Univ. Sussex (UK); and Caltech, JPL, NHSC, Univ. Colorado (USA). This development has been supported by national funding agencies: CSA (Canada); NAOC (China); CEA, CNES, CNRS (France); ASI (Italy); MCINN (Spain); SNSB (Sweden); STFC (UK); and NASA (USA). PACS has been developed by a consortium of institutes led by MPE (Germany) and including UVIE (Austria); KU Leuven, CSL, IMEC (Belgium); CEA, LAM (France); MPIA (Germany); INAF-IFSI/OAA/OAP/OAT, LENS, SISSA (Italy); IAC (Spain). This development has been supported by the funding agencies BMVIT (Austria), ESA-PRODEX (Belgium), CEA/CNES (France), DLR (Germany), ASI/INAF (Italy), and CICYT/MCYT (Spain).

References

- Alvarez-Gutierrez, R.H., Stutz, A.M., Law, C.Y., et al., 2021, *ApJ*, 908, 86
- Andree-Labsch, S., Ossenkopf-Okada, V., Röllig, M., *A&A*, 2017, 598, 2
- Asplund, M., Grevesse, N., Sauval, A. J., 2005, *ASPC*, 336, 25
- Bertoldi, F., 1989, *ApJ*, 346, 735
- Bisbas, T., Haworth, T.J., Barlow, M.J., et al., 2015, *MNRAS*, 454, 2828
- Black, J.H., van Dishoeck, E.F., 1987, *ApJ*, 322, 412
- Cauley, P.W., Johns-Krull, C.M., 2014, *ApJ*, 797, 112
- Cohen, M., Jones, B.F., Walker, H.J., 1989, *ApJ* 341, 908
- Comerón, F., Torra, J., 1999, *A&A*, 349, 605

- Comerón, F., Pasquali, A., Rodighiero, G., et al., 2002, A&A, 389, 874
- Comerón, F., Djupvik, A., Schneider, N., Pasquali, A., 2020, A&A, 644, 62
- Cubick, M., Stutzki, J., Ossenkopf, V., et al., 2008, A&A, 488, 623
- Dale, J.E., Haworth, T.J., Bressert, E., 2015, MNRAS, 450, 1199
- Diaz-Miller, R.I., Franco, J., Shore, S.N., 1998, ApJ, 501, 192
- Draine, B.T., 1978, ApJS, 36, 595
- Djupvik, A.A., Comerón, F., Schneider, N., 2017, A&A, 599, 37
- de Graauw, T., Helmich, F. P., Philips, T. G., et al. 2010, A&A, 518, L4
- Fuente, A., Martín-Pintado, J., Bachiller, R., et al., 2002, A&A, 387, 977
- Gahm, G.F., Carlqvist, P., Johansson, L.E., Nikolic, S., 2006, A&A, 545, 201
- Gritschneider, M., Naab, T., Walch, S. et al., 2009, ApJ, 694, L26
- Goldsmith, P., Langer, W.D., Pineda, P., Velusamy, T., 2012, ApJS, 203, 13
- Griffin, M., Abergel, A., Abreau, A., et al., 2010, A&A, 518, L3
- Guevara, C., Stutzki, J., Ossenkopf-Okada, V., et al., 2010, A&A, 636, 16
- Habing, H.J., 1968, Bull. Astron. Inst. Netherlands, 19, 421
- Hester, J.J., Scowen, P.A., Sankrit, R., 1996, AJ, 111, 2349
- Heyminck, S., Graf, U.U., Güsten, R., Stutzki, J., et al., 2012, A&A, 542, L1
- Hollenbach, D., Kaufman, M. J., Neufeld, D., et al., 2012, ApJ, 754, 105
- Hsieh, C., Arcre, H.G., Maradones, D., et al., 2021, ApJ, 908, 92
- Johnstone, D., Hollenbach, D., Bally, J., 1998, ApJ, 499, 758
- Kaufman, M.J., Wolfire, M.G., Hollenbach, D.J., Luhman, M.L., 1999, ApJ, 527, 795
- Knödlseeder, J., 2000, A&A, 360, 539
- Kronberger, M., Teutsch, P., Alessi, B., et al., 2006, A&A, 447, 921
- Kumar, M., Keto, E., Clerkin, E., 2006, A&A, 449, 1033
- Langer, W. D., Penzias, A. A., 1990, ApJ, 357, 477
- Lebouteiller, V., Cormier, D., Madden, S. C., et al., 2012, A&A, 548, 91
- Langer, W.D., Velusamy, T., Pineda, J., et al., 2010, A&A, 521, L17
- Le Boulrot, J., Pineau Des Forets, G., Roueff, E., Flower D.R., 1993, A&A, 267, 233
- Lefloch, B., Lazareff, B., 1994, A&A, 289, 559
- Lefloch, B., Cernicharo, J., Pardo, J. R., 2008, A&A, 489, 157
- Levshakov, S.A., Reimers, D., Henkel, C., A&A, 586, 126
- Lim, B., Nazé, Y., Gosset, E., 2020, MNRAS, 490, 440
- Mathematica Version 12.1, Wolfram Research. Inc., Champaign, IL, 2020
- Meijerink, R., Spaans, M., 2005, A&A, 436, 397
- Miao, J., White, G.J., Nelson, R.P., et al., 2006, MNRAS, 369, 143
- Miao, J., White, G.J., Thompson, M.A., et al., 2009, ApJ, 692, 382
- Motte, F., Zavagno A., Bontemps S., Schneider N., et al., 2010, A&A, 518, L77
- Moura, T., Alencar, S.H.P., Sousa, A.P., et al., 2020, MNRAS, 494,
- Pilbratt, G.L., Riedinger, J.R., Passvogel, T., et al. 2010, A&A, 518, 1
- Poglitsch, A., Waelkens, C., Geis, N., et al., 2010, A&A 518, L2
- Polehampton, E. T., Baluteau, J.-P., Swinyard, B. M., 2005, A&A, 437, 957
- Reipurth, B., Schneider, N., 2008, Handbook of star-forming regions, ASP, p.37
- Risacher, C., Güsten, R., Stutzki, J., et al., 2016, A&A, 595, 34
- Rodríguez, L.F., Zapata, L.A., Dzib, S.A., 2014, ApJL, 793, L21
- Röllig, M., Ossenkopf, V., Jeyakumar, S., et al., 2006, A&A, 451, 917
- Röllig, M., Abel, N. P., Bell, T., et al., 2007, A&A, 467, 187
- Röllig, M., Szczerba, R., Ossenkopf, V., Glück, C., 2013, A&A, 549, 85
- Roelfsema, P. R., Helmich, F. P., Teyssier, D., et al. 2012, A&A, 537, 17
- Rygl, K., Brunthaler, A., Sanna, A., et al. 2012, A&A 539, 79
- Schneider, N., Bontemps, S., Simon, R., et al., 2006, A&A, 458, 855
- Schneider, N., Bontemps, S., Simon, R., et al., 2011, A&A, 529, 1
- Schneider, N., Güsten, R., Tremblin, P., et al., 2012, A&A, 542, L18
- Schneider, N., Bontemps, S., Motte, F., et al., 2016, A&A, 591, 40
- Schneider, N., Röllig, M., Simon, R., et al., 2018, A&A, 617, 45
- Schneps, M.H., Ho, P.T.P., Barrett, A.H., 1980, ApJ, 240, 84
- Shirley, Y.L., 2015, PASP, 127, 299
- Simon-Diaz, S., Stasinska, G., 2011, A&A, 526, 48
- Sofue, Y., 2020, MNRAS, 492, 5966
- Sternberg, A., Dalgarno, A., 1995, ApJS, 99, 565
- Swinyard, B.M., Polehampton, E.T., Hopwood, R., et al., 2014, MNRAS, 440, 3658
- Tielens, A.G.G.M., Hollenbach, D., 1985, ApJ, 291, 722
- Tremblin, P., Audit, E., Minier, V., Schneider, N., 2012a, A&A, 538, 31
- Tremblin, P., Audit, E., Minier, V., Schmidt, W., Schneider, N., 2012b, A&A, 546, 33
- Tremblin, P., Minier, V., Schneider, N., et al., 2013, A&A, 560, 19
- Valtchanov, I., Hopwood, R., Bendo, G., et al., 2018, MNRAS, 475, 321
- Wakelam, V., Herbst, E., 2008, ApJ, 680, 371
- Weingartner, J.C., Draine, B.T., 2001, ApJ, 548, 296
- White, G.J., Lefloch, B., Fridlund, C.V.M., et al., 1997, A&A, 323, 931
- White, G.J., Nelson, R.P., Holland, W.S., et al., 1999, A&A, 342, 233
- Wright, N., Drew, J.E., Mohr-Smith, M., 2015, MNRAS, 449, 741
- Wolfire, M.G., McKee, C.F., Hollenbach, D., Tielens, A.G.G.M., 2003, ApJ, 587, 278
- Wu, R., Polehampton, E.T., Etxaluze, M., et al., 2013, A&A, 556, 116

Appendix A: PACS and SPIRE spectroscopy**Appendix B: PDR model input parameters****Table B.1.** Overview of the most important model parameters (see also Andree-Labsch et al. (2017)). All abundances are given with respect to the total H abundance.

Model Input Parameters		
He/H	0.0851	(1)
O/H	$4.47 \cdot 10^{-4}$	(2)
C/H	$2.34 \cdot 10^{-4}$	(2)
$^{13}\text{C}/\text{H}$	$3.52 \cdot 10^6$	(3) ^a
$^{18}\text{O}/\text{H}$	$8.93 \cdot 10^{-7}$	(4) ^b
N/H	$8.32 \cdot 10^{-5}$	(2)
S/H	$7.41 \cdot 10^{-6}$	(2)
F/H	$6.68 \cdot 10^{-9}$	(2)
Z	1	solar metallicity
ζ_{CR}	$2 \cdot 10^{-16} \text{ s}^{-1}$	CR ionisation rate (5)
R_{V}	5.5	visual extinction/reddening (7,8)
σ_{D}	$8.41 \cdot 10^{-22} \text{ cm}^2$	UV dust cross section per H (8)
$\langle A(\lambda)/A_{\text{V}} \rangle$	2.40	mean FUV extinction
τ_{UV}	$2.2 A_{\text{V}}$	FUV dust attenuation
ν_b	1 km s^{-1}	Doppler width
n_0	$10^{3 \dots 7} \text{ cm}^{-3}$	total surface gas density
M	$10^{-3 \dots 3} M_{\odot}$	cloud mass
χ	$10^{0 \dots 6}$	FUV intensity w.r.t. (6) ^c
α	1.5	density power law index
R_{core}	$0.2 R_{\text{tot}}$	size of constant density core
$N_{\text{tot}}/A_{\text{V}}$	$1.89 \cdot 10^{21} \text{ cm}^{-2}$	(8)

References. (1) Asplund et al. (2005); (2) Simon-Diaz & Stasinska (2011); (3) Langer & Penzias (1990); (4) Polehampton et al. (2005); (5) Hollenbach et al. (2012); (6) Draine (1978); (7) Röllig et al. (2013); (8) Weingartner & Draine (2001a).

Notes. ^(a) based on a $^{12}\text{C}/^{13}\text{C}$ ratio of 67 ^(b) based on a $^{16}\text{O}/^{18}\text{O}$ ratio of 500 ^(c) $\chi = 1.71 G_0$ where G_0 is the mean ISRF from (Draine 1978).

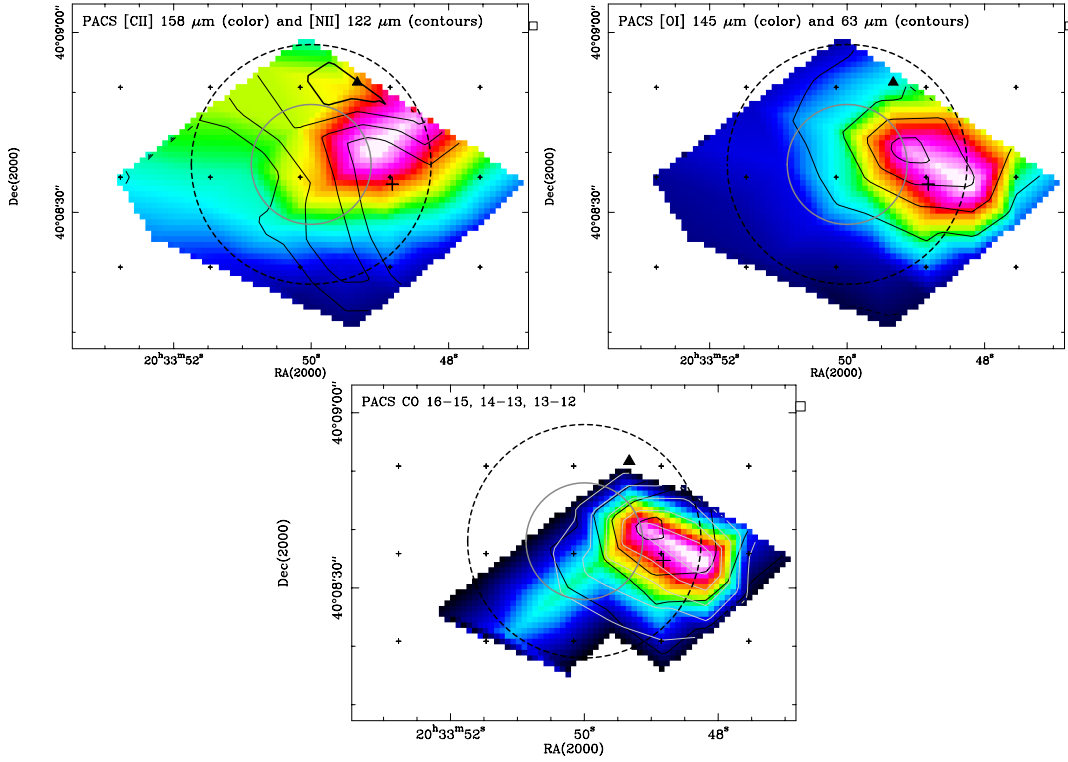


Fig. A.1. Various overlays of PDR lines observed with PACS. The colour range for the PACS [C II] data (top left) is 20 to 211 K km s⁻¹, contours (1, 2, 3, 4 K km s⁻¹) of [N II] emission are overlaid. The colour range for the PACS [O I] 145 μm data (top right) is 0 to 85 K km s⁻¹, contours (10, 50, 90, 130, 170 K km s⁻¹) of PACS [O I] 63 μm emission are overlaid. The colour range for the PACS CO 13→12 data (bottom) is 0 to 16 K km s⁻¹, black contours (1, 4, 7, 11 K km s⁻¹) of PACS CO 16→15 emission, and grey contours (5 to 25 by 5 K km s⁻¹) of PACS CO 14→13 emission are overlaid. The 'finger' of emission in CO 13→12 emission is probably an artefact since it is not visible in the CO 16→15 and 14→13 lines. The black triangle indicates the double system (Star A) of which at least one is a Herbig Be star, the white rectangle points to Star B with a B0.5 B1.5 spectral type, and the large black cross marks Star C, a resolved binary of which one is late O or early B star. The solid grey circle has a size of 20'' and the dashed one of 40''. This is the position for the flux determination for PDR modelling.

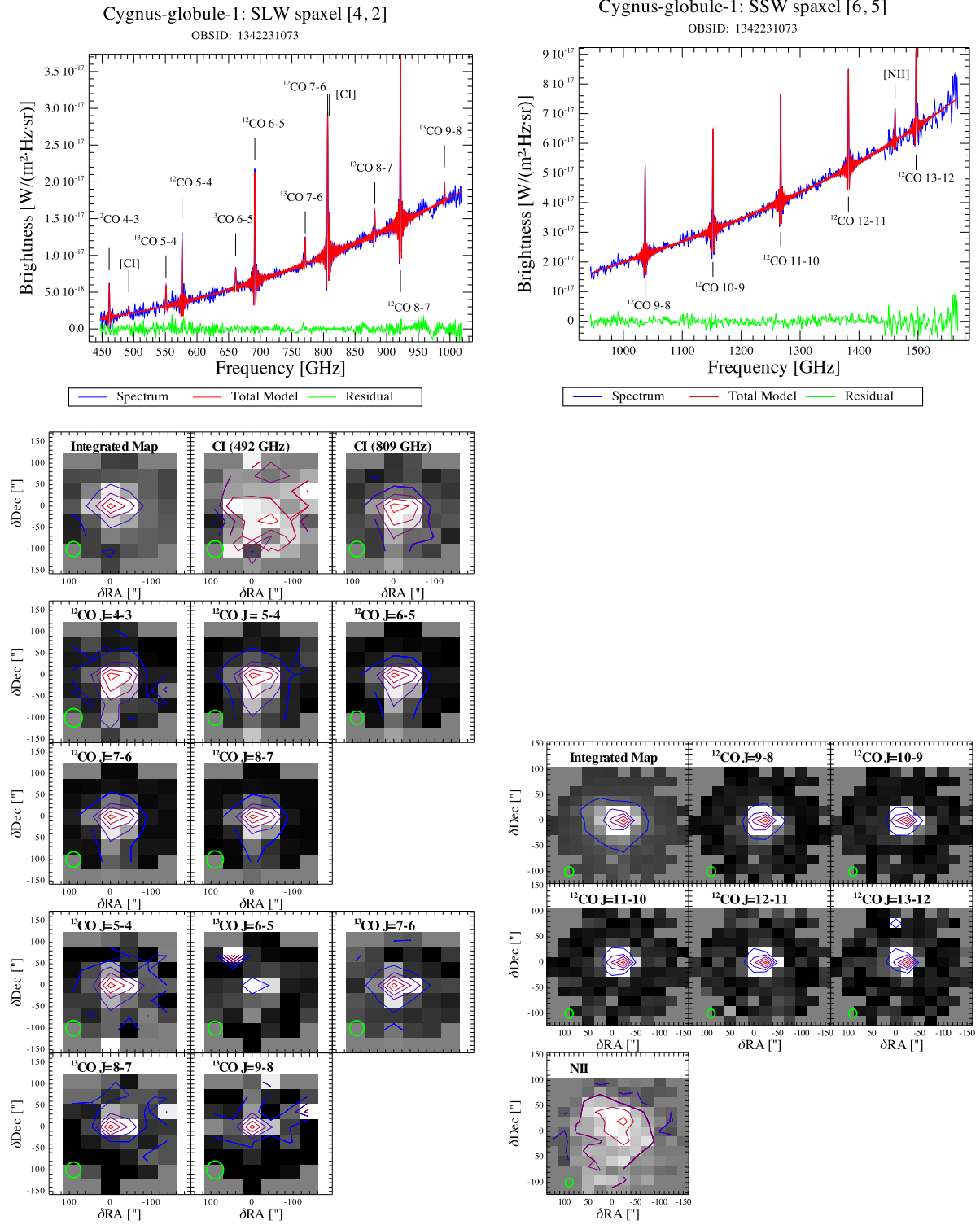


Fig. A.2. SPIRE spectroscopy results for the globule head. Top: FTS spectrum (blue) and line fit (red) for one spaxel of the SPIRE spectrometer for SLW (left) and SSW (right). The positions of the spectral lines included in the fit are indicated. Bottom: Full SPIRE spectral maps showing the CO-ladder and the [C I] and [N II] lines. The intensity scale has been set relative to the peak brightness in each map with contour levels at 0.1, 0.3, 0.5, 0.7 and 0.9 of the peak (from blue to red). The SPIRE beam size varies between 31–43'' for SLW and 16–20'' for SSW (Swinyard et al. 2014).

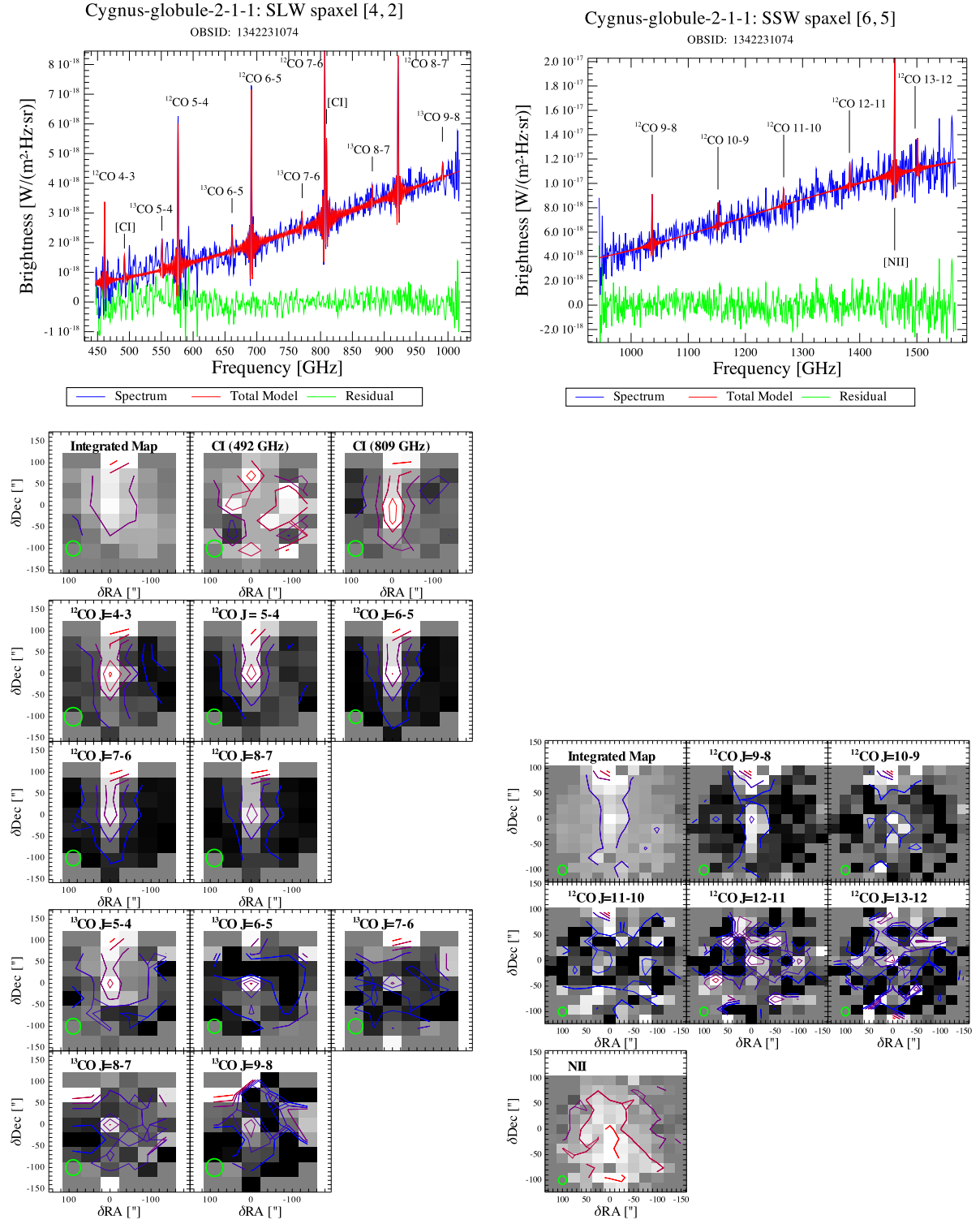


Fig. A.3. SPIRE spectroscopy results for the globule tail. Details are the same as Fig. A.2.